RESEARCH ARTICLE SUMMARY

IN SITU SEQUENCING

Expansion sequencing: Spatially precise in situ transcriptomics in intact biological systems

Shahar Alon*, Daniel R. Goodwin*, Anubhav Sinha*, Asmamaw T. Wassie*, Fei Chen*, Evan R. Daugharthy†, Yosuke Bando, Atsushi Kajita, Andrew G. Xue, Karl Marrett, Robert Prior, Yi Cui, Andrew C. Payne, Chun-Chen Yao, Ho-Jun Suk, Ru Wang, Chih-Chieh (Jay) Yu, Paul Tillberg, Paul Reginato, Nikita Pak, Songlei Liu, Sukanya Punthambaker, Eswar P. R. Iyer, Richie E. Kohman, Jeremy A. Miller, Ed S. Lein, Ana Lako, Nicole Cullen, Scott Rodig, Karla Helvie, Daniel L. Abravanel, Nikhil Wagle, Bruce E. Johnson, Johanna Klughammer, Michal Slyper, Julia Waldman, Judit Jané-Valbuena, Orit Rozenblatt-Rosen, Aviv Regev, IMAXT Consortium, George M. Church‡§, Adam H. Marblestone§, Edward S. Boyden‡§

INTRODUCTION: Cells and tissues are made up of diverse molecular building blocks, organized with nanoscale precision over extended length scales. Newly developed techniques that enable highly multiplexed, nanoscale, and subcellular analysis of such systems are required. Although much progress has been made on methods for multiplexed RNA imaging, these methods have been limited in their spatial precision, especially in the context of three-dimensional systems such as tissues. Because of this limitation, interrogation of tissues has been performed with either high spatial resolution or high molecular multiplexing capacity, but not both.

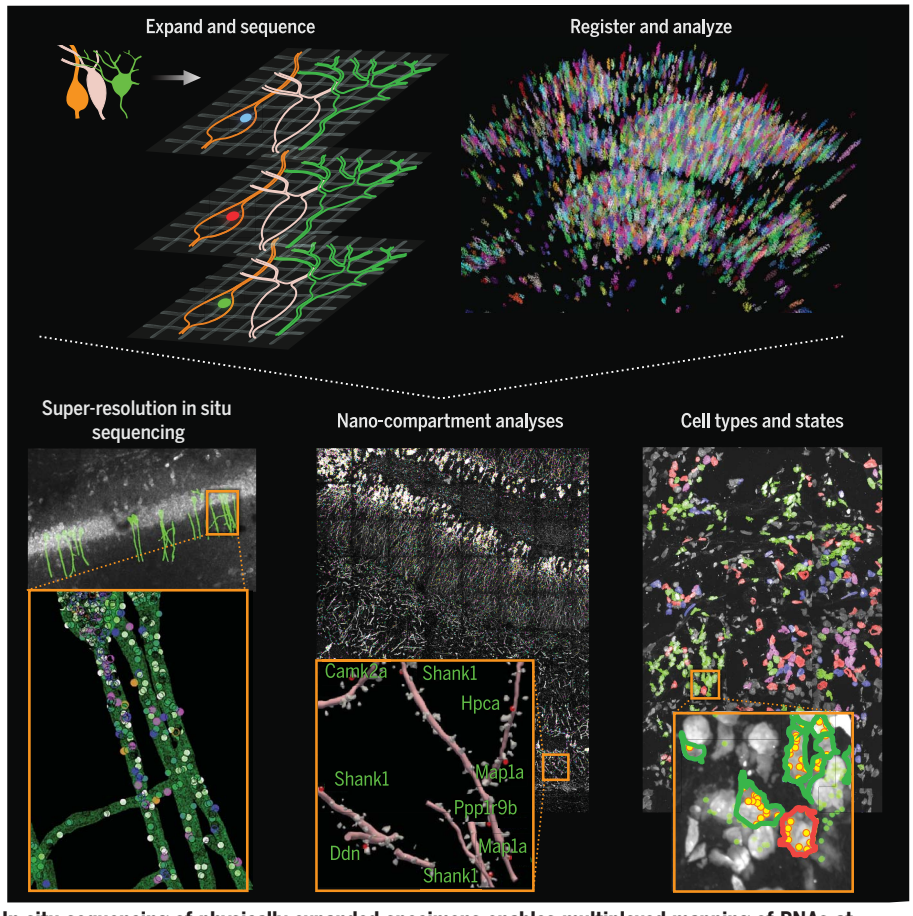

In situ sequencing of physically expanded specimens enables multiplexed mapping of RNAs at nanoscale, subcellular resolution throughout intact tissues. (Top) Schematics of physical expansion and in situ sequencing (left) and image analysis (right). (Bottom) Characterization of nanoscale transcriptomic compartmentalization in mouse hippocampal neuron dendrites and spines (left and middle) and maps of cell types and states in a metastatic human breast cancer biopsy (right).

RATIONALE: We reasoned that physically expanding specimens by adapting expansion microscopy could help support spatially precise in situ sequencing. The physical expansion of specimens provides two benefits: First, it enables ordinary microscopes to achieve nanoscale effective resolution. Second, by anchoring RNA molecules to a polymer network, digesting away other molecules, and then expanding the polymer in water, RNAs become more accessible. By creating a chemical process that enables enzymatic reactions to proceed in expanded specimens, we enabled in situ fluorescent sequencing of RNA with high spatial precision, which we term expansion sequencing (ExSeq). We developed both untargeted (i.e., not restricted to a predefined set of genes) and targeted versions of ExSeq.

RESULTS: Using untargeted ExSeq, we showed the presence of transcripts that retain their introns, transcription factors, and long noncoding RNAs in mouse hippocampal neuron dendrites. Using targeted ExSeq, we observed layer-specific cell types across the mouse visual cortex and RNAs in nanoscale compartments of hippocampal pyramidal neurons, such as dendritic spines and branches. We found that spines could exhibit distributions of mRNAs different from those exhibited by adjacent dendrites. Moreover, we found patterns of similarity between the dendritic profiles of RNAs in different types of hippocampal neurons. In a human metastatic breast cancer biopsy, we mapped how cell types expressed genes differently as a function of their distance from other cell types, identifying, for example, cellular states of immune cells specific to when they were close to tumor cells.

CONCLUSION: ExSeq enables highly multiplexed mapping of RNAs—from nanoscale to system scale—in intact cells and tissues. We explore how RNAs are preferentially targeted to dendrites and spines of neurons, suggesting RNA localization principles that may generalize across different cell types. We also examine gene expression differences in cell types as a function of their distance from other cell types in the context of a human cancer, which may yield insights into future therapeutic approaches that take cellular interactions into account. ■

The list of author affiliations is available in the full article online.
*These authors contributed equally to this work.
†This author made key and essential contributions to the early stages of the project.
‡Corresponding author. Email: gchurch@genetics.med.harvard.edu (G.M.C.); edboyden@mit.edu (E.S.B.)
§These authors contributed equally to this work.
Cite this article as S. Alon *et al.*, *Science* **371**, eaax2656 (2021). DOI: 10.1126/science.aax2656

READ THE FULL ARTICLE AT
https://doi.org/10.1126/science.aax2656

RESEARCH ARTICLE

IN SITU SEQUENCING

Expansion sequencing: Spatially precise in situ transcriptomics in intact biological systems

Shahar Alon[1,2,3]*, Daniel R. Goodwin[1,2]*, Anubhav Sinha[1,2,4]*, Asmamaw T. Wassie[1,2,5]*, Fei Chen[1,6]*, Evan R. Daugharthy[7,8]†‡, Yosuke Bando[1,9], Atsushi Kajita[10], Andrew G. Xue[1], Karl Marrett[10], Robert Prior[10], Yi Cui[1,2], Andrew C. Payne[1,6], Chun-Chen Yao[1,6], Ho-Jun Suk[1,2,4], Ru Wang[1,2], Chih-Chieh (Jay) Yu[1,2,5], Paul Tillberg[1]§, Paul Reginato[1,5,6,7,8], Nikita Pak[1,2,11], Songlei Liu[7,8], Sukanya Punthambaker[7,8], Eswar P. R. Iyer[8], Richie E. Kohman[7,8], Jeremy A. Miller[12], Ed S. Lein[12], Ana Lako[13], Nicole Cullen[13], Scott Rodig[13], Karla Helvie[14], Daniel L. Abravanel[6,15,16], Nikhil Wagle[14], Bruce E. Johnson[14], Johanna Klughammer[6], Michal Slyper[6], Julia Waldman[6], Judit Jané-Valbuena[6], Orit Rozenblatt-Rosen[6], Aviv Regev[6,17,18], IMAXT Consortium[19]¶, George M. Church[7,8]#**, Adam H. Marblestone[1]**††, Edward S. Boyden[1,2,5,17,18,20]#**

Methods for highly multiplexed RNA imaging are limited in spatial resolution and thus in their ability to localize transcripts to nanoscale and subcellular compartments. We adapt expansion microscopy, which physically expands biological specimens, for long-read untargeted and targeted in situ RNA sequencing. We applied untargeted expansion sequencing (ExSeq) to the mouse brain, which yielded the readout of thousands of genes, including splice variants. Targeted ExSeq yielded nanoscale-resolution maps of RNAs throughout dendrites and spines in the neurons of the mouse hippocampus, revealing patterns across multiple cell types, layer-specific cell types across the mouse visual cortex, and the organization and position-dependent states of tumor and immune cells in a human metastatic breast cancer biopsy. Thus, ExSeq enables highly multiplexed mapping of RNAs from nanoscale to system scale.

Tissues are made of cells of many different types and states that are regulated by and contribute to the cells' spatial organization. Multiplexed measurements of the locations and identities of RNA molecules within cells has been useful for exploring these relationships (*1*–*13*). Furthermore, mapping the subcellular locations of RNAs is important for understanding diverse biological processes (*14*, *15*), such as how RNAs in dendritic spines help regulate synaptic function (*16*–*19*).

Imaging RNAs within such compartments, and throughout detailed cellular morphologies, requires nanoscale precision. Such precision is not easily achieved in tissues with current multiplexed optical methods to image RNA. No method can currently perform multiplexed imaging of RNA within tissues in the context of nanoscale cellular morphology. Even though sequential fluorescence in situ hybridization (seqFISH+) allows high-resolution imaging of RNA molecules, it cannot resolve the detailed cellular and tissue context with nanoscale precision (*20*).

Ideally one would be able to perform the enzymatic reactions of sequencing in situ with high multiplexing capacity, while providing for fast nanoscale imaging of cellular and tissue context. Here, we present a toolbox for the untargeted (i.e., not restricted to a predefined list of gene targets) and targeted in situ sequencing of RNAs within intact tissues, in the context of nanoscale cellular morphology.

Adapting expansion microscopy to improve in situ sequencing

We created an untargeted in situ sequencing technology that enables the sequencing of arbitrary RNAs in detailed cellular and tissue contexts. Untargeted approaches have the potential to discover spatially localized sequence variants, such as splice variants and retained introns (*21*). Fluorescent in situ sequencing (FISSEQ) enables such data to be acquired from cultured cells but was not fully demonstrated in tissues (*22*). Therefore, we adapted the chemistry of expansion microscopy (ExM) (*23*, *24*) to separate RNAs from nearby molecules. We reasoned that this may facilitate the chemical access needed for in situ sequencing within tissues. We also expected that the resolution boost from ExM would enable high–spatial resolution mapping of RNAs and their cellular and tissue context on conventional microscopes.

In FISSEQ, untargeted in situ sequencing of RNA is performed to amplify RNA into nanoballs of cDNA (or amplicons), which contain many copies of an RNA sequence (*22*, *25*). These sequences are interrogated in situ with standard next-generation sequencing chemistries on a fluorescence microscope. In ExM (*23*), we isotropically separate gel-anchored biomolecules of interest by an ~4× linear expansion factor, which facilitates both nanoscale imaging with conventional optics and better chemical access to the separated biomolecules (*24*). ExM enables better resolution of normally densely packed RNA transcripts for in situ hybridization imaging (*26*, *27*).

Expanding specimens is expected to benefit FISSEQ by dividing the effective size of the FISSEQ amplicon (200 to 400 nm) (*22*) by the expansion factor. This reduces the packing density of amplicons and facilitates their tracking over many rounds of sequencing. We adapted ExM chemistry to enable FISSEQ in expanded tissues. In particular, the anchoring (Fig. 1A, i), polymerization (Fig. 1A, ii), and expansion (Fig. 1A, iii) steps, which separate RNAs for nanoscale imaging (*26*), result in charged carboxylic acid groups throughout the swellable gel. This suppresses the enzymatic reactions required for FISSEQ (fig. S1). We thus stabilized expanded specimens by re-embedding them in uncharged gels (*26*) and then chemically treated samples to result in a neutral charge environment (fig. S1). We expected that this would allow FISSEQ signal amplification (Fig. 1A, iv) and readout (Fig. 1A, v and vi, and Fig. 1B) steps to proceed.

In situ sequencing involves many rounds of adding fluorescent oligonucleotides (*22*). Accordingly, we established an automated sequencing system (*28*). Because the resultant datasets consist of a series of three-dimensional

[1]Department of Media Arts and Sciences, MIT, Cambridge, MA, USA. [2]McGovern Institute, MIT, Cambridge, MA, USA. [3]Faculty of Engineering, Gonda Brain Research Center and Institute of Nanotechnology, Bar-Ilan University, Ramat Gan, Israel. [4]Harvard-MIT Program in Health Sciences and Technology, MIT, Cambridge, MA, USA. [5]Department of Biological Engineering, MIT, Cambridge, MA, USA. [6]Broad Institute of MIT and Harvard, Cambridge, MA, USA. [7]Department of Genetics, Harvard Medical School, Boston, MA, USA. [8]Wyss Institute for Biologically Inspired Engineering, Boston, MA, USA. [9]Kioxia Corporation, Minato-ku, Tokyo, Japan. [10]Fixstars Solutions Inc, Irvine, CA, USA. [11]Department of Mechanical Engineering, MIT, Cambridge, MA, USA. [12]Allen Institute for Brain Science, Seattle, WA, USA. [13]Center for Immuno-Oncology (CIO), Dana-Farber Cancer Institute, Boston, MA, USA. [14]Center for Cancer Genomics, Dana-Farber Cancer Institute, Boston, MA, USA. [15]Department of Medical Oncology, Dana-Farber Cancer Institute, Boston, MA, USA. [16]Department of Cell Biology, Harvard Medical School, Boston, MA, USA. [17]Koch Institute for Integrative Cancer Research, Department of Biology, MIT, Cambridge, MA, USA. [18]Howard Hughes Medical Institute, Chevy Chase, MD, USA. [19]CRUK IMAXT Grand Challenge Consortium, Cambridge, UK. [20]Department of Brain and Cognitive Sciences, MIT, Cambridge, MA, USA.
*These authors contributed equally to this work. †This author made key and essential contributions to the early stages of the project. ‡Present address: ReadCoor, part of 10x Genomics, Cambridge, MA, USA. §Present address: Janelia Research Campus, Ashburn, VA, USA. ¶The IMAXT Consortium collaborators and their affiliations are listed in the supplementary materials.
#Corresponding author. Email: gchurch@genetics.med.harvard.edu (G.M.C.); edboyden@mit.edu (E.S.B.) **These authors contributed equally to this work. ††Present address: Federation of American Scientists, Washington, DC, USA.

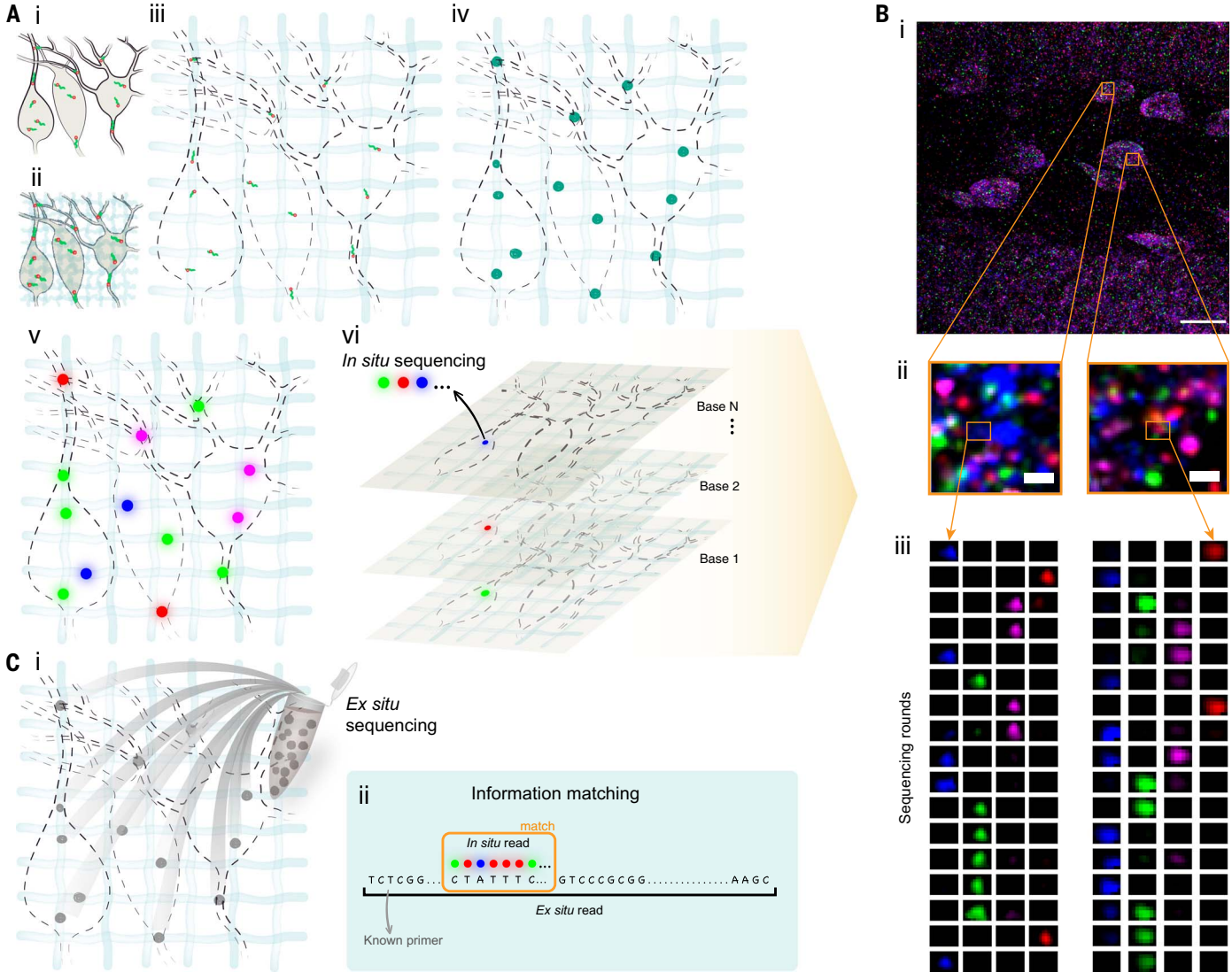

Fig. 1. Untargeted ExSeq concept and workflow. (**A**) ExSeq schematic. (i) A specimen is fixed, and RNA molecules (green) are bound by an anchor (orange). (ii) The specimen is embedded in a swellable gel material (light blue, not to scale), mechanically softened, and then expanded with water (iii). RNA molecules are anchored to the gel. (iv) RNA molecules are reverse transcribed and amplified using FISSEQ. (v) In situ sequencing. Colored dots indicate the colors used in the sequencing chemistry. (vi) In each sequencing round, colors (blue, magenta, green, and red) reveal the current base of the cDNA. (**B**) Example of ExSeq from a 50-μm-thick slice of mouse dentate gyrus. (i) One sequencing round, with two zoomed-in regions (ii) and puncta histories obtained over the course of 17 rounds of in situ sequencing (iii). (**C**) Ex situ sequencing. (i) After in situ sequencing, cDNA amplicons are eluted from the sample and resequenced ex situ with next-generation sequencing. (ii) In situ reads are matched to their longer ex situ counterparts, focusing on unique matches, augmenting the effective in situ read length. Scale bars in (B) are 17 μm in (i) (in biological, i.e., pre-expansion units used throughout, unless otherwise indicated) and 700 nm in (ii).

(3D) images, one for each successive base sequenced, we created a software pipeline (fig. S2) (*29*). This software can align—across images from many rounds—the puncta for each expressed gene to within one pixel (validated in figs. S3 and S4). Finally, puncta are segmented and bases are called (Fig. 1B, iii).

In situ sequencing has previously been limited to short reads of 5 to 30 bases (*10*, *11*, *22*). This limitation reflects laser-induced damage during imaging (*25*) and dependence of the signal for a given cycle on signals from previous cycles (known as phasing), which is caused by incomplete enzymatic reactions (*30*). Alignment of such short reads to the genome is challenging (*31*). Moreover, short reads do not easily capture mRNA complexity, such as alternative splicing.

Accordingly, we added a follow-on round of ex situ classical next-generation sequencing (Fig. 1C, i) (*28*). Notably, the random nature of untargeted sequencing (*28*) results in the creation of distinct molecular identifiers from the in situ sequenced region of the amplified cDNA (fig. S5). This allows us to use ex situ information as a dictionary to align and directly interpret the in situ reads (Fig. 1C, ii, and fig. S5A, bottom panel).

In total, 92% of all matches, and 97% of the matches aligned against nonribosomal RNA, were strictly unique. We removed the handful of in situ reads that matched to more than one ex situ library entry (*28*). Thus, one in situ read matches one ex situ library entry (fig. S5C). This allowed us to explore sequence variations in mRNA, such as alternative splicing, using the longer ex situ matched reads (fig. S6).

Biological validations of ExSeq

Expansion sequencing (ExSeq) produced data from a variety of specimens (tables S1 to S5), including mouse brain (Fig. 1B), *Caenorhabditis*

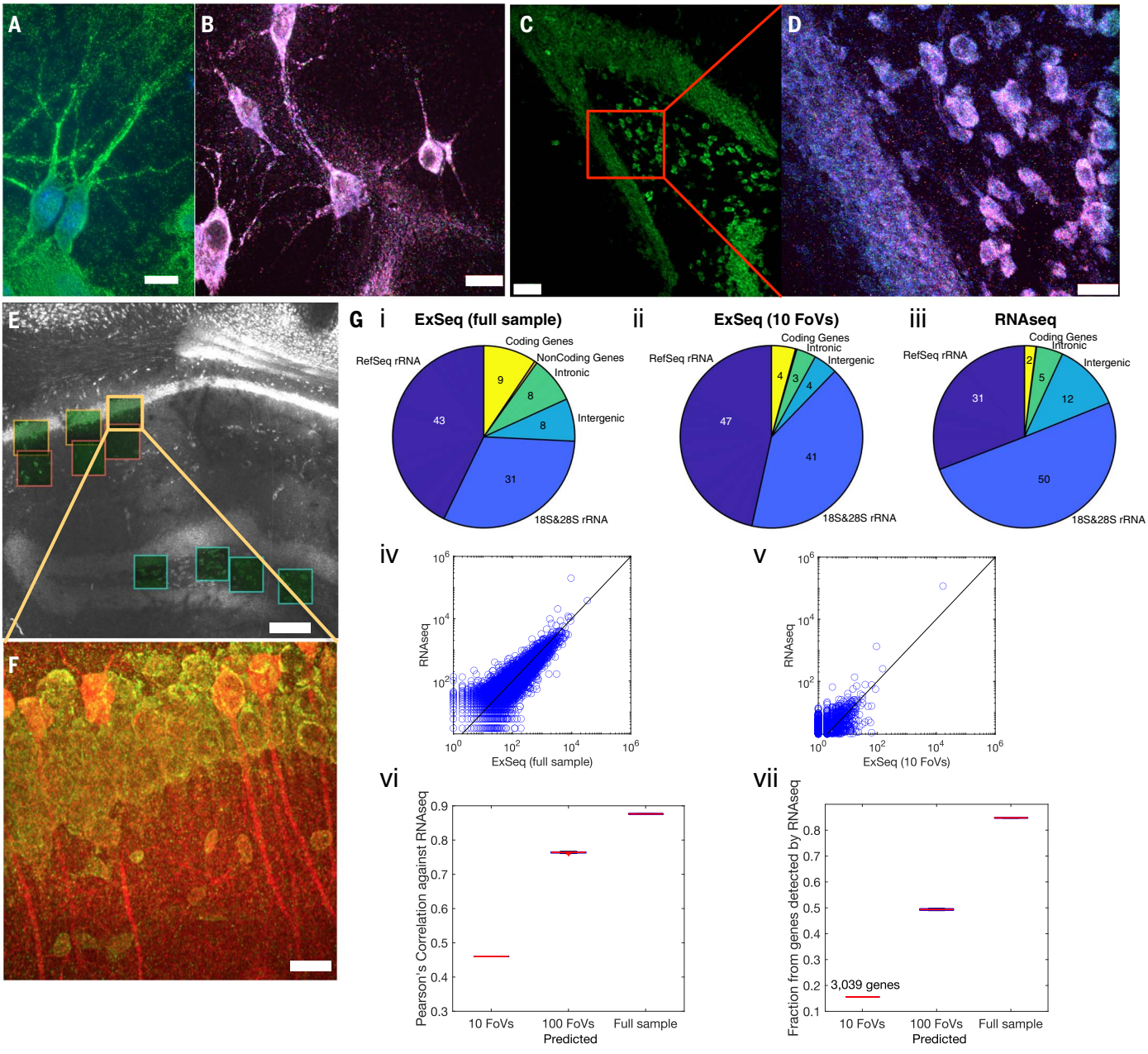

Fig. 2. In situ sequencing in cells and tissues with untargeted ExSeq. (**A**) Example of ExSeq library preparation in hippocampal culture (green, hybridization probe against amplified cDNA; blue, DAPI). (**B**) Maximum intensity projection of one sequencing round in hippocampal culture; color scheme as in Fig. 1B. (**C**) Low-magnification image of ExSeq library preparation in a 15-μm slice of mouse hippocampus (green, hybridization probe against amplified cDNA). (**D**) Maximum intensity projection of a higher-magnification image of the specimen in (C), focusing on one sequencing round; color scheme as in Fig. 1B. (**E**) Low-magnification image of ExSeq library preparation in a 50-μm slice of mouse hippocampus. Fields of view (FoVs) acquired with a higher-magnification objective are shown as green squares. White indicates hybridization probe against amplified cDNA. (**F**) Maximum intensity projection of one FoV of (E), with antibody staining after in situ sequencing (red, antibody against YFP; specimen from a Thy1-YFP mouse; green, hybridization probe against amplified cDNA). (**G**) Sequence analysis of ExSeq specimen shown in (E). (i to iii) RNA content obtained with ExSeq—either using ex situ sequencing data from the entire slice (i) or using ex situ data that correspond to in situ reads observed within the FoVs of (E) (ii)—is comparable to the RNA content of an adjacent slice obtained with standard RNA-seq (iii). Numbers inside the pie chart represent percentages of the total. (iv) Agreement between the normalized expression levels of all well-annotated genes (RefSeq genes) using RNA-seq and ExSeq with full ex situ sequencing data as in (i). (v) As in (iv), but using the 10 acquired FoVs, as in (ii). (vi) Pearson's correlation between the log-transformed expression of RefSeq genes using ExSeq and using RNA-seq, as a function of the number of acquired FoVs [estimated by sampling from the full ex situ sequencing data to simulate the number of expected reads for 100 FoVs; (*28*)]. The value for the 100 FoVs is plotted using the MATLAB boxplot function. The central mark indicates the median, and the bottom and top edges of the box indicate the 25th and 75th percentiles, respectively. (vii) Fraction of RefSeq genes detected using ExSeq versus RNA-seq, as a function of the number of acquired FoVs (estimated by sampling from the full ex situ sequencing data to simulate the number of expected reads for 100 FoVs). Scale bars in (A) to (D) and (F) are 13 μm and in (E) are 130 μm. Deconvolution was used in (D) and (F) (*28*).

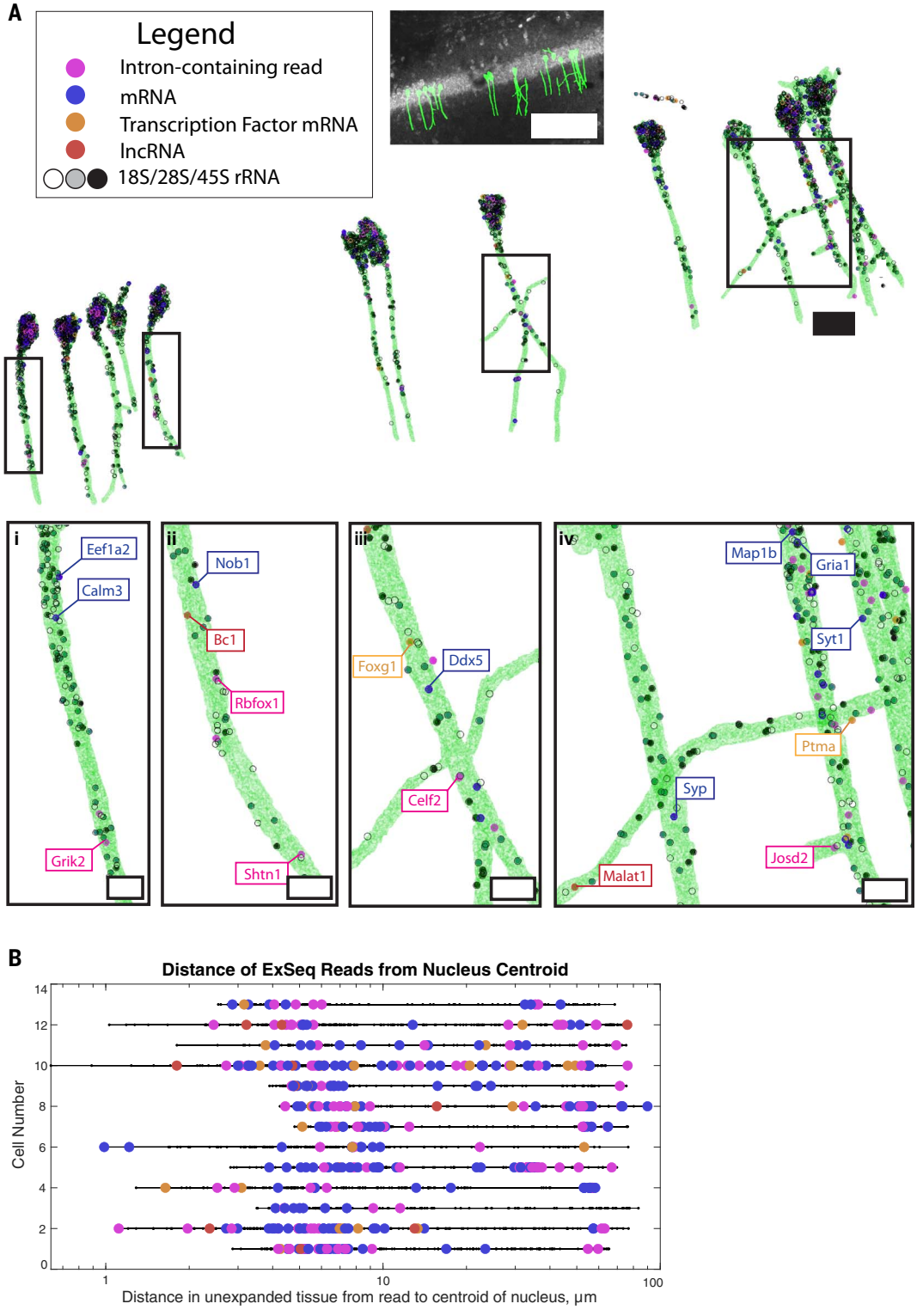

Fig. 3. Untargeted ExSeq enables mapping of RNAs and their variants in dendrites of neurons. (**A**) 3D render of Thy1-YFP CA1 neuronal morphology as determined by YFP antibody staining, containing RNA types as indicated. (i to iv) Zoomed-in dendritic regions (boxed above). Scale bars in top, middle, and bottom rows are 100, 20, and 5 µm, respectively. (**B**) Euclidean distance, relative to the center of the cell body, of sequencing reads for neurons in (A). Color code is as in (A).

elegans (fig. S7A), *Drosophila* embryos (fig. S7B), and HeLa cells (fig. S7C). To validate ExSeq, we used the following mouse specimens: cultured hippocampal neurons (Fig. 2, A and B, and fig. S8), a 15-µm-thick hippocampal slice (Fig. 2, C and D), and a 50-µm-thick hippocampal slice (Fig. 2, E and F). To improve the efficiency of cDNA circularization, we restricted the size of cDNA fragments to ~100 bases long, so ex situ Illumina reads typically contained several repeats of a given cDNA fragment that were, on average, 76 bases long (fig. S6).

Antibody staining after in situ sequencing, as with previous ExM-related protocols (*32*), enabled visualization of specific proteins. This was demonstrated by staining with antibodies against yellow fluorescent protein (YFP) in a Thy1-YFP mouse (*33*) to visualize in situ sequencing reads in neural morphology (Fig. 2F).

As a validation of ExSeq, we performed RNA sequencing (RNA-seq) with random primers on a 50-µm-thick hippocampal slice adjacent to the 50-µm-thick ExSeq specimen (Fig. 2, E and F). As expected for total RNA analysis,

most of the RNA detected in both cases was ribosomal. We observed overall agreement between the RNA types obtained with both methods (Fig. 2G, i to iii), although ExSeq exhibited a slightly higher percentage of coding RNA (4 to 9% with ExSeq versus 2% with RNA-seq). Gene ontology analysis revealed expected functional enrichments for this specimen, including categories such as synapse, neuron projection, and hippocampus (fig. S9 and table S6).

In FISSEQ, highly abundant genes were underrepresented—for example, genes involved in translation and splicing (*22*). By contrast, we did not observe this detection bias with ExSeq (*28*). The expression levels of well-annotated genes (genes from the RefSeq database) using RNA-seq and ExSeq were highly correlated (Pearson's correlation coefficient, $r = 0.89$) (Fig. 2G, iv, and fig. S8C).

The correlation between ExSeq and RNA-seq increased with the ExSeq volume imaged. For example, 10 microscope volumes (each 350 μm by 350 μm by 100 μm in size after expansion, and ~100 μm by 100 μm by 28 μm pre-expansion) resulted in a Pearson's correlation coefficient of $r = 0.47$ (Fig. 2G, v; Student's t test, $P = 9 \times 10^{-164}$) comparable to recent targeted in situ sequencing methods (*34*). Larger volumes, simulated by sampling (*28*), yielded higher correlations (Fig. 2G, vi). With 10 volumes, 3039 genes were detected, making up ~16% of all the genes detected in the sample through RNA-seq, again increasing with the volume sampled (Fig. 2G, vii). Thus, ExSeq is able to report on genome-wide expression in situ in an untargeted, highly multiplexed way.

Subcellular pinpointing of transcript locations in neurons

We next sought to utilize the improved spatial resolution of ExSeq to pinpoint RNAs relative to antibody-stained morphology. We traced 13 hippocampal CA1 pyramidal neurons (*28*). We analyzed the locations of RNAs inside identified neurons with a custom 3D viewer (Fig. 3 and fig. S10) (*28*). The number of sequencing reads per neuron was 229 ± 74 (mean ± standard deviation used throughout) including ribosomal RNA (rRNA), and 30 ± 14 for nonribosomal RNA, for cell bodies and dendrites imaged up to ~100 μm from the cell body. Not including rRNAs, 326 RefSeq genes were observed in these imaged volumes. These numbers are comparable to those obtained by the original FISSEQ protocol (*25*), applied to cultured cell lines.

Neurons contain one nucleus versus thousands of synapses. This raises the question of whether the splicing of mRNAs, such as those that contribute to synaptic function, is regulated in a spatially dependent manner along dendritic trees (*35*). We examined reads that corresponded to intronic regions and observed that, although 70% of such reads were located at the soma, introns in YFP-containing dendritic projections could be found as far down the dendrite as we looked, consistent with previous studies (*36*, *37*). For example, glutamate ionotropic receptor kainate type subunit 2 (*Grik2*), which encodes a receptor subunit involved in excitatory glutamatergic neurotransmission, appears in our data in dendrites with a retained intron (Fig. 3A, i). The *Grik1* subunit had been identified earlier as a dendritically targeted, intron-retaining sequence (*36*, *38*). Dendritic splicing of glutamate receptor subunit RNAs may contribute to the regulation of the state or plasticity of excitatory synapses. In fact, splicing in dendrites has been characterized previously in cultured neurons (*39*).

The long sequencing reads (fig. S6) and untargeted nature of ExSeq also allowed for mapping of alternative splicing in situ. We quantified the expression of known alternative splicing isoforms with ExSeq versus RNA-seq. The two methods were highly correlated (Pearson's $r = 0.944$; fig. S11A). Using only 10 confocal microscope fields of view, of sizes described above, we detected 112 sequencing reads that corresponded to known alternative splicing events. Of these sequencing reads, 67% revealed the expressed alternative splicing isoforms, including ribosomal protein S24 (*Rps24*) and microtubule-associated protein 2 (*Map2*) (fig. S11B). We also identified what are perhaps previously unidentified isoforms, for example for the gene spectrin beta (*Sptbn1*) (fig. S11B).

ExSeq provides the ability to locate these alternative splicing events in space. As an example, isoforms of *Map2*, a key dendritic protein (*40*), and the transcription factor *Cux1*, which is involved in dendrite and spine formation (*41*), could be localized to the neuronal soma outside of the nucleus (fig. S10, neurons 9 and 7, respectively, and fig. S11B).

Many genes may have unappreciated connections to neuronal signaling inside dendritic trees. mRNAs for specific transcription factors have been identified inside dendrites (*42*), for example MAX dimerization protein (*Mga*) (*43*) (fig. S10, neuron 6). However, the full complement of dendritically localized transcription factors in any neuron type is unknown.

In our hippocampus sample (table S2), 914 of the known 1675 mouse transcription factors (RIKEN transcription factor database) were detected by ExSeq. This included 32 reads localized within YFP-expressing cells and 11 reads in the dendrites of these cells. These reads include forkhead box protein G1 (*Foxg1*), which is involved with neural development (*44*), and prothymosin alpha (*Ptma*), which is involved in learning and memory and neurogenesis (*45*) (Fig. 3A, iii, and Fig. 3A, iv). We also found long noncoding RNAs (lncRNAs) and protein coding genes with unknown function in dendrites (Fig. 3A). For example, *Bc1* (Fig. 3A, ii) is a lncRNA from an RNA polymerase III transcript that complexes with proteins to form a ribonucleoprotein particle. *Bc1* is dendritically localized (*46*) and is involved with activity-dependent synaptic regulation (*47*). Additionally, *Malat1* (Fig. 3A, iv) has roles in neural growth and synaptogenesis, but its localization had not been determined in hippocampal tissue (*48*, *49*).

We localized genes that had been found in dendrites of CA1 pyramidal cells at the protein level but had not been mapped at the mRNA level, such as γ-aminobutyric acid (GABA) type A receptor gamma2 subunit (*Gabrg2*) (fig. S10, neuron 2) (*50*). Thus, ExSeq allows us to expand our knowledge of dendritically localized genes of known function, which may point to previously unknown regulatory mechanisms for their gene products. Furthermore, we identified transcripts encoding genes of unknown function in the hippocampus (e.g, *Nob1*; Fig. 3A, ii) (*51*), which may contribute to their functional analysis.

To more systematically understand how the types and identities of transcripts varied with location along a dendrite, we measured the distance from each read to the centroid of its corresponding neuron's cell body (Fig. 3B). These measurements reveal the positions of RNAs encoding for transcription factors, intron-containing reads, and lncRNAs up to 100 μm from the soma. To follow up with a more in-depth examination of specific genes, we next generated a targeted form of ExSeq.

Targeted ExSeq

Untargeted sequencing enables transcriptome-wide exploration of localized RNAs, including rare variants and those of unknown function. However, the diversity of possible reads generated by untargeted methods lead to a lower per-gene copy number of detected molecules and a larger number of biochemical and imaging cycles to distinguish among reads. Targeted methods, by contrast, detect a smaller predefined set of genes and are applicable to mapping cell types and states, mapping their spatial relationships in situ, and visualizing subcellular gene regulation.

An ideal technology for targeted multiplexed RNA mapping would satisfy the following list of criteria. First, it should have sufficient yield (probability of detecting a present molecule) to detect low copy number transcripts such as transcription factors or sparse RNA molecules. Second, the technology should have resolution below the diffraction limit both laterally and axially to resolve nanoscale morphological features, such as dendritic spines in neurons.

Third, the method should provide the ability to image both RNAs and proteins and to work with 3D tissues to localize RNAs in biological contexts. Finally, the method should work with various tissue types, including human tissues. We thus developed a targeted version of ExSeq to match these specifications (tables S7 and S8).

In targeted ExSeq, oligonucleotide padlock probes bearing barcodes hybridize to transcripts (*11*, *52*). Amplicons are then generated for readout through in situ sequencing of the barcodes (Fig. 4A and fig. S12). The inefficient (*22*) reverse transcription step required by untargeted in situ sequencing (*11*, *22*, *53*) is circumvented by the binding and ligation of padlock probes on each targeted transcript using PBCV-1 DNA ligase (also known as SplintR ligase). This enzyme can ligate DNA on an RNA template ~100× faster than T4 DNA ligase (*52*, *54*–*57*). After circularization and rolling circle amplification, the barcodes are sequenced in situ. As barcodes are sequenced across multiple rounds of imaging, the number of identifiable molecular targets scales exponentially with the number of imaging rounds.

We explored the performance of targeted ExSeq in a variety of contexts (table S5). To validate the yield, hybridization chain reaction (HCR) v3.0–amplified expansion FISH (ExFISH) and targeted ExSeq were sequentially performed for the same genes in expanded HeLa cells (*26*, *58*). Targeted ExSeq exhibited an mRNA detection yield of ~62% (Pearson's r = 0.991) relative to HCRv3.0–amplified ExFISH (Fig. 4B and tables S9 to S11), which has a detection efficiency of ~70% in tissue (*26*). For comparison, single-cell RNA sequencing (scRNA-seq) captures ~10% of mRNA (*59*, *60*).

Cell type mapping with spatial context in the visual cortex

We mapped the cell types of the mouse primary visual cortex, for which scRNA-seq data–based classification of cell types has been performed (*61*). We designed a panel of probes targeting 42 genes (tables S9 and S10) that mark key excitatory and inhibitory neuron types. We performed targeted ExSeq of these 42 genes across a coronal section of the primary visual cortex of a Thy1-YFP mouse over a volume of 0.933 mm by 1.140 mm by 0.02 mm, sequencing 265,347 reads (Fig. 4C, top, and table S12).

The spatial distribution of ExSeq reads recapitulated spatial distributions in the Allen in situ hybridization (ISH) atlas (fig. S13). Transcripts known to express in the same cell type appeared in similar positions—for example, in parvalbumin-positive (Pvalb$^+$) interneurons (PV interneurons), parvalbumin (*Pvalb*), vesicular inhibitory amino acid transporter (*Slc32a1*), and glutamate decarboxylase 2 (*Gad2*) transcripts colocalized (Fig. 4C, inset). By contrast, seizure protein 6 homolog (*Sez6*) transcripts, associated with excitatory neurons in deep cortical layers [as well as vasoactive intestinal peptide (VIP$^+$) interneurons] was not colocalized with *Pvalb*, *Slc32a1*, and *Gad2* transcripts (Fig. 4C, inset).

Segmenting cells (fig. S14) (*28*) yielded a total of 1915 cells containing a total of 220,783 reads. Out of these, 1154 cells with at least 50 reads each (177 ± 127 reads per cell) were analyzed. We k-means clustered expression profiles and embedded them into a low-dimensional space using t-distributed stochastic neighbor embedding (t-SNE) (*62*) (Fig. 4D). Clusters were identified with known markers (*28*), such as those corresponding to excitatory neurons (labeled "Ex," and subannotated by their layer location) and inhibitory neurons (annotated with relevant cell type markers). Clusters expressed marker genes consistent with prior studies (*61*) (fig. S15).

We compared our results with a previous study of scRNA-seq of the mouse primary visual cortex (*28*, *61*) (Fig. 4E). We observed the canonical layer-by-layer stratification of excitatory neurons in the visual cortex (Fig. 4F and fig. S16). The nine ExSeq clusters of excitatory neurons corresponded, with slightly different groupings, to seven scRNA-seq clusters of excitatory neurons (Fig. 4E). We found inhibitory neuron ExSeq clusters that matched one-to-one to scRNA-seq clusters. For example, two somatostatin interneuron clusters found across the layers of the cortex—the SST cluster expressing Unc-13 homolog C (cluster SST Unc13c) and the SST cluster expressing *Chondrolectin* (cluster SST Chodl)—appeared prominently in both datasets (Fig. 4, F and G). Some ExSeq clusters of inhibitory neurons mapped onto multiple scRNA-seq clusters. For example, two ExSeq clusters, which we denoted PV and GABAergic (–PV), mapped onto multiple scRNA-seq clusters (Fig. 4E).

Such poolings of scRNA-seq clusters into ExSeq clusters (and vice versa) are likely caused by the smaller number of cells analyzed with ExSeq versus scRNA-seq, the small number of markers interrogated, and the use of a simple k-means algorithm for clustering. Some substructure is visible in the t-SNE plot for the cluster GABAergic (–PV) (Fig. 4D). This suggests that alternative clustering approaches, for instance utilizing morphological criteria or protein markers, could be devised in the future to yield more-precise delineations of cell types.

We varied the parameters used for cell segmentation of the ExSeq dataset and for clustering of the single-cell dataset and found the above conclusions to be robust (figs. S17 and S18). Nonneuronal cells (e.g., glial cells) did not highly express the interrogated markers and were likely nonspecifically clustered with other cell types.

As described (*61*, *63*), the layer-specific excitatory neuron transcription factor marker genes homeobox protein cut-like 2 (*Cux2*), RAR-related orphan receptor beta (*Rorb*), fasciculation and elongation protein zeta-2 (*Fezf2*), and forkhead box protein P2 (*Foxp2*) were expressed in cortical layers 2/3 (L2/3), L4, L5b, and L6, respectively (Fig. 4, E and F, and fig. S15). We used the clusters featuring these markers to segment the cortex into layers (fig. S14D) so that the cell types within each layer could be quantified (Fig. 4G; raw counts, fig. S19). Each cluster of inhibitory neurons was dispersed across layers (Fig. 4G and fig. S19), consistent with earlier work (*61*, *63*). Thus, targeted ExSeq enables sensitive RNA detection across circuit-relevant volumes of tissue and enables cell types to be analyzed in spatial context.

Nanoscale RNA compartmentalization in mouse hippocampal neurons

We next used targeted ExSeq to explore nanoscale RNA compartmentalization within neurons of the mouse hippocampus, where dendritic RNAs are implicated in synaptic plasticity and learning (*64*–*66*). We traced YFP in neurons to identify dendrites and spines and targeted 34 transcripts previously found in CA1 neuron dendrites for sequencing (*67*). Spines were not observed in the untargeted ExSeq hippocampus data because the antibody staining was performed after sequencing, which resulted in weaker staining, whereas here, antibody staining was performed pre-expansion (*28*).

We performed four rounds of in situ sequencing to localize these transcripts on 170 fields of view (1.7 mm by 1 mm by 0.02 mm total; table S5). This sequencing spanned a coronal section containing subfields of the hippocampus and yielded 1.2 million reads, 90,000 of which localized within YFP-expressing neurons (Fig. 5A and table S13). The distributions of expressed genes were similar to those reported in the Allen Brain Atlas in situ hybridization dataset (fig. S20).

Using the YFP signal, we segmented the CA1 pyramidal neurons and dentate gyrus granule cells (although the spines and axons of the latter exhibited low signal-to-noise ratios and were not analyzed further). We found transcripts in dendrites (CA1, DG), spines (CA1), and, to a much smaller extent, axons (CA1) (Fig. 5B). In 106,000 spines examined, we found 730 reads in dendritic spines (each spine had one RNA, except for one that had two). Through simulations (fig. S21), we concluded that it was unlikely that this sparsity of distribution was caused by chemical artifacts of the ExSeq procedure.

In CA1 neurons, as expected, genes such as the postsynaptic density protein dendrin (*Ddn*), the synaptic plasticity-associated gene *Camk2a*, and the postsynaptic scaffolding protein SH3

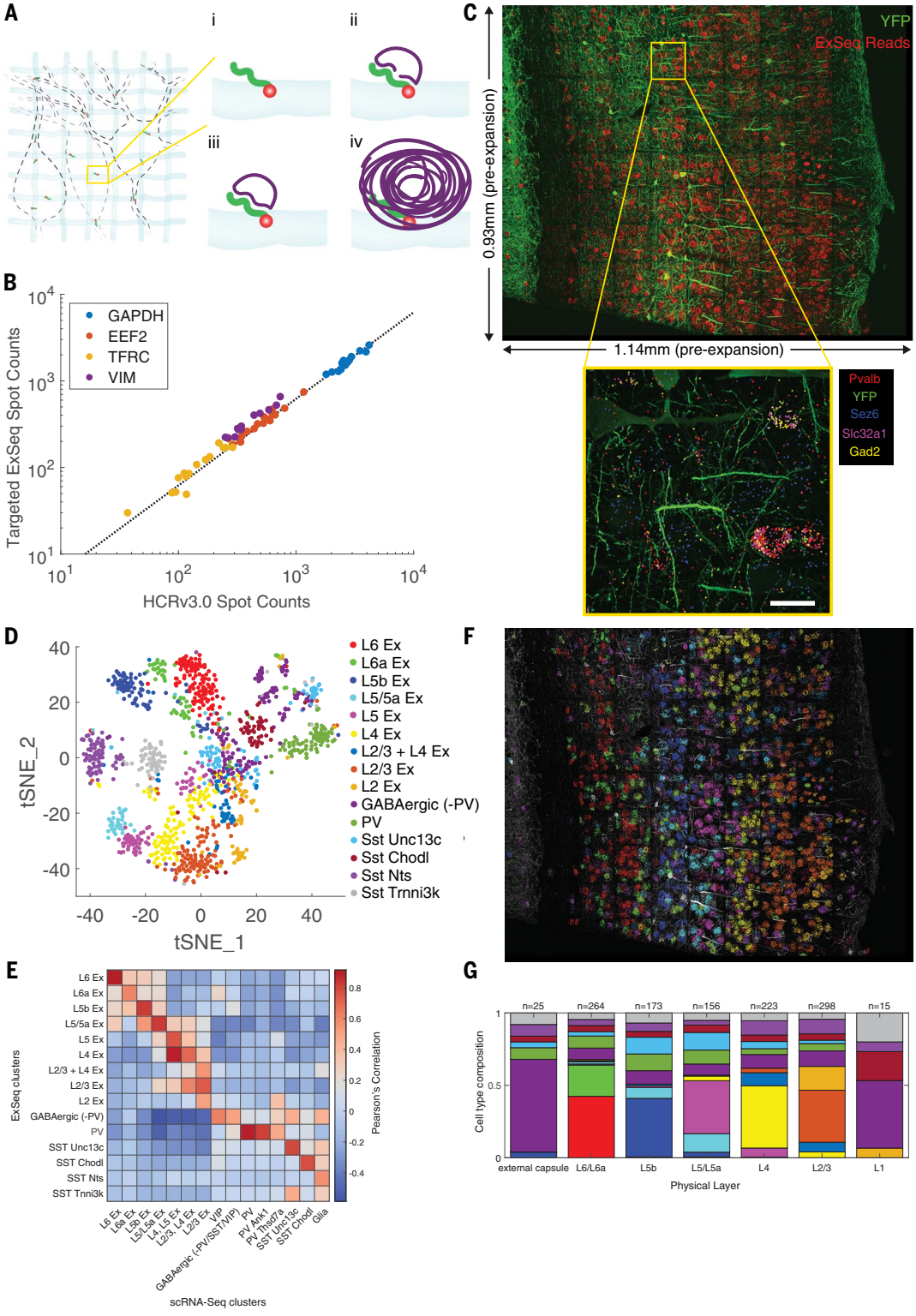

Fig. 4. Targeted ExSeq of transcripts specifying neuron types of mouse primary visual cortex. (**A**) Targeted ExSeq library preparation: (i) RNA anchoring and expansion, (ii) padlock probe hybridization, (iii) probe ligation, and (iv) rolling circle amplification. (**B**) Amplicon counts for targeted ExSeq versus HCRv3.0–amplified ExFISH for the same transcript in the same HeLa cell (60 cells) (slope, 0.62; Pearson's r = 0.991). (**C**) Targeted ExSeq of 42 cell type marker genes in Thy1-YFP mouse visual cortex. (Top) Maximum intensity projection image showing targeted ExSeq reads (red) and YFP (green). (Bottom) Localization of marker genes *Pvalb* (red), *Sez6* (cyan), *Slc32a1* (magenta), and *Gad2* (yellow) with YFP (green). (**D**) Targeted ExSeq gene expression profiles of 1154 cells clustered into 15 cell types. Cluster legend and colors apply to (D), (F), and (G). (**E**) Heatmap showing Pearson's correlation between clusters identified in targeted ExSeq versus a prior scRNA-seq study (*61*). (**F**) Spatial organization of cell types identified in (D). Cell-segmented reads are shown, colored by cluster assignment, and overlaid on YFP (white). (**G**) Layer-by-layer cell-type composition across segmented cortical layers. Scale bar in (C) (bottom) is 20 μm (pre-expansion).

and multiple ankyrin repeat domains 1 (*Shank1*) were prominent in dendrites. The neuronal calcium sensor *Hpca* and the synaptic glutamate receptor *Gria1* were amongst the most abundant in cell bodies (Fig. 5C). In spines, we found *Shank1*, Adenylyl cyclase 1 (*Adcy1*), and kinesin family member 5a (*Kif5a*) to be amongst the most abundant transcripts. We found that the distribution of reads in cell bodies, apical dendrites, basal dendrites, apical dendritic spines, and basal dendritic spines was each statistically different from the others (bootstrapped two-sample Kolmogorov-Smirnov test, $P < 0.001$), except for apical versus basal spines, which were not different from each other (Fig. 5C, iii). This suggests a common set of spine RNAs and spine RNA trafficking principles throughout these neurons.

We validated these observations through bulk RNA sequencing from hippocampal slices adjacent (±100 μm coronally) to the

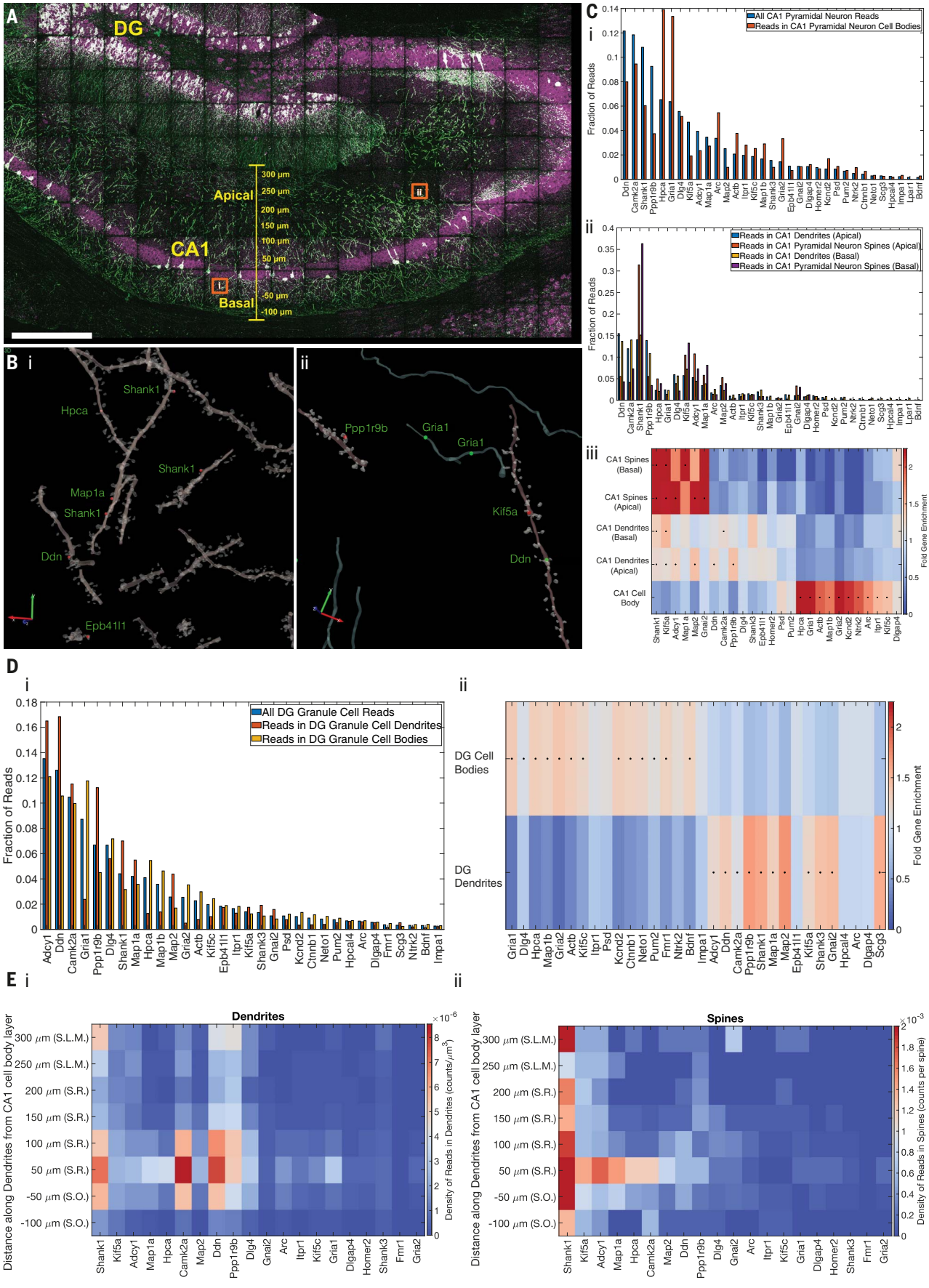

Fig. 5. Targeted ExSeq characterization of nanoscale transcriptomic compartmentalization in mouse hippocampal neuron dendrites and spines. (**A**) Confocal image showing targeted ExSeq of a 34-panel gene set across a slice of mouse hippocampus. Green indicates YFP, magenta indicates reads identified with ExSeq, and white indicates reads localized within YFP-expressing cells. DG, dentate gyrus; CA1, CA1 region of hippocampus. (**B**) 3D reconstruction of dendrites, spines, and axons showing reads localized in spines (red dots) and processes (green dots) for regions indicated by orange boxes in (A). (**C**) The abundance of transcripts in cellular compartments of CA1 pyramidal neurons: (i) abundance of transcripts in all cellular compartments versus cell bodies, (ii) abundance of transcripts in apical and basal dendrites and spines, and (iii) heatmap showing the enrichment of transcripts in apical and basal dendritic and spine compartments of CA1 pyramidal neurons, versus cell bodies. Asterisks indicate statistically significant enrichment (bootstrapped $P < 0.001$). (**D**) The abundance of transcripts in cellular compartments of dentate gyrus (DG) granule cells: (i) abundance of transcripts in the cell bodies and dendrites of DG granule cells and (ii) heatmap showing enrichment of transcripts in compartments of DG granule cells. Asterisks indicate statistically significant enrichment (bootstrapped $P < 0.001$). (**E**) Plots showing the density of transcripts in the dendrites (i) and spines (ii) of CA1 pyramidal neurons along the apical-basal axis (Euclidean distance) of CA1, including regions S.R. (stratum radiatum), S.O. (stratum oriens), and S.L.M. (stratum lacunosum moleculare). Scale bar in (A) is 300 μm, and those in (B) are 2 and 3 μm in (i) and (ii), respectively, shown as red and green arrows in (B) (pre-expansion).

section used for targeted ExSeq. We observed a high level of correlation between in situ sequencing results and bulk RNA sequencing results (Pearson's $r = 0.85$; fig. S22). For the genes studied through both untargeted and targeted versions of ExSeq, we observed high correlation between the read counts (Pearson's $r = 0.68$; fig. S22 and table S13). Using these genes, we estimated the yield of untargeted ExSeq to be 0.6% versus targeted ExSeq (table S13).

Specific genes were significantly (bootstrapped, $P < 0.001$) enriched in specific CA1 neuronal compartments (Fig. 5C). Transcripts for *Shank1*, *Kif5a*, *Adcy1*, *Map1a*, *Map2*, and *Gnai2*, were highly enriched in spines and, to a smaller extent, in apical and basal dendrites compared with cell bodies, perhaps pointing to a process through which these transcripts are enriched the closer they get to synapses. Many of these genes serve structural roles in spines and dendrites (*68*–*70*). On the other hand, a distinct set of genes, including *Hpca*, *Gria1*, *ActB*, and *Map1b* among others, were highly enriched in cell bodies compared with dendrites or spines, consistent with an earlier study (*67*). Notably, *Arc*, whose RNA is known to be dendritically targeted in plasticity contexts, was enriched in cell bodies, consistent with the highly regulated nature of its presence in dendrites (*71*, *72*). Additionally, a few genes, such as *Camk2a* and *Ddn*, were enriched in dendrites compared with both spines and cell bodies, consistent with earlier work (*67*).

In dentate gyrus dendrites, we found transcripts similar to those found in CA1 apical and basal dendrites such as *Shank1*, *Map2*, and *Ppp1r9b* (Fig. 5D). Across the entire 34-gene set, we observed similar dendritic localizations of RNAs in dentate gyrus granule cells versus CA1 pyramidal neurons (Pearson's $r = 0.91$; fig. S23). This similarity raises the possibility that there may be general rules, applicable to multiple neuron types, that govern the dendritic transport of specific RNAs.

Transcripts exhibit varied distributions along dendrites (*67*). We found that most transcripts within dendrites were close (±50 μm) to the cell body layer, and their density decayed rapidly toward distal regions of dendrites, similar to previous observations for these genes (*67*) (Fig. 5E, i, and fig. S24).

Some transcripts, such as *Shank1*, *Ddn*, and *Ppp1r9b*, were present in distal regions of dendrites. When we quantified the presence of transcripts within spines along dendrites, however, we observed a markedly different distribution (Fig. 5E, ii, and fig. S24). For most transcripts found in spines among those in our probe set, their highest density occurred close to the cell body layer. However, spine-localized *Shank1* transcripts exhibited a strong presence throughout spines in proximal and distal regions of dendrites in both apical and basal directions. *Kif5a* and *Adcy1*, to a lesser extent, were also found in the spines of distal dendrites. Thus, although spines are directly connected to dendritic branches, they can exhibit markedly different mRNA distributions.

ExSeq mapping of cell type relationships in cancer

We next explored how ExSeq might reveal spatial patterns of gene expression in the context of cancer biology and immunology. One key question is to understand how tumor microenvironments, including the state of immune cells, govern tumor growth, metastasis, and treatment resistance (*73*). Multiplexed spatial mapping of RNA performed in human tissues to date has not achieved high enough resolution for single-cell quantification, let alone subcellular resolution (*34*, *74*, *75*) (table S7).

A core biopsy was taken from a patient with metastatic breast cancer infiltration into the liver, and 297 tumor-related genes of interest (*28*) were profiled. We resolved 1.15 million reads, including 771,904 reads in 2395 4′,6-diamidino-2-phenylindole (DAPI)–segmented nuclei (Fig. 6A, counts in table S14). The high 3D spatial resolution of ExSeq allowed the detection of 516 RNA reads inside nuclear structures <1 μm in size—possibly nucleoplasmic bridges, which are challenging structures to resolve in tissue (*76*) (fig. S25).

Expression clustering of DAPI-segmented cells (*28*, *77*) revealed the expected mixture of cell types, including tumor, immune (T cell, B cell, and macrophage), and fibroblast cell clusters, characterized with known biomarkers. These biomarkers include members of the immunoglobulin family (*IGHG1*, *IGHG4*, and *IGKC*) found in B cells and genes known to be expressed in metastatic breast cancer [progesterone receptor (*PGR*) (*78*), epidermal growth factor receptor (*EGFR*) (*79*), and aldehyde dehydrogenase 1 family member A3 (*ALDH1A3*) (*80*)] (Fig. 6B).

Tumor and nontumor cells were highly intermixed (Fig. 6C). We examined spatial colocalizations (proximity within 20 μm) between cell types [Fig. 6D; results were robust to distance parameter value (fig. S26)]. Different B cell clusters tended to colocalize in space, consistent with previous observations (*81*). B cell clusters exhibited statistically significant [using bootstrapping (*28*)] colocalizations to all the other cell clusters (Fig. 6D) except for one tumor cluster expressing the gene marker *PGR* (tumor PGR). This is consistent with B cells directly interacting with tumor cells and macrophages, with such interactions contributing to humoral responses in the microenvironment (*81*, *82*). Our analysis also indicates other cell type colocalizations—for example between fibroblast clusters and macrophage, T cell, and tumor clusters (Fig. 6D). Such mappings thus may help illuminate the role of fibroblasts in supporting leukocyte aggregation at sites of cancer (*83*) or the spatial distributions of fibroblast cell types in cancers (*84*).

We finally analyzed whether one cell type could express genes differently as a function of physical proximity to another cell type. For example, one cell might change state depending on physical contact or close proximity to another cell. For each pair of cell clusters that exhibited colocalization, we searched gene expression differences between specific cells that were close (i.e., within 20 μm) versus not close using bootstrapping (*28*). Hypoxia-inducible factor (*HIF1A*) was overexpressed more than fivefold in ALDH1A3-positive tumor cells when they were in close proximity to HSPG2-positive fibroblasts (Fig. 6E, ii). Given that HIF1A serves as a proxy of hypoxic environments and is a microenvironmental cue for tumor cell maintenance (*85*), ExSeq maps may be helpful for further probing such relationships. The mRNA

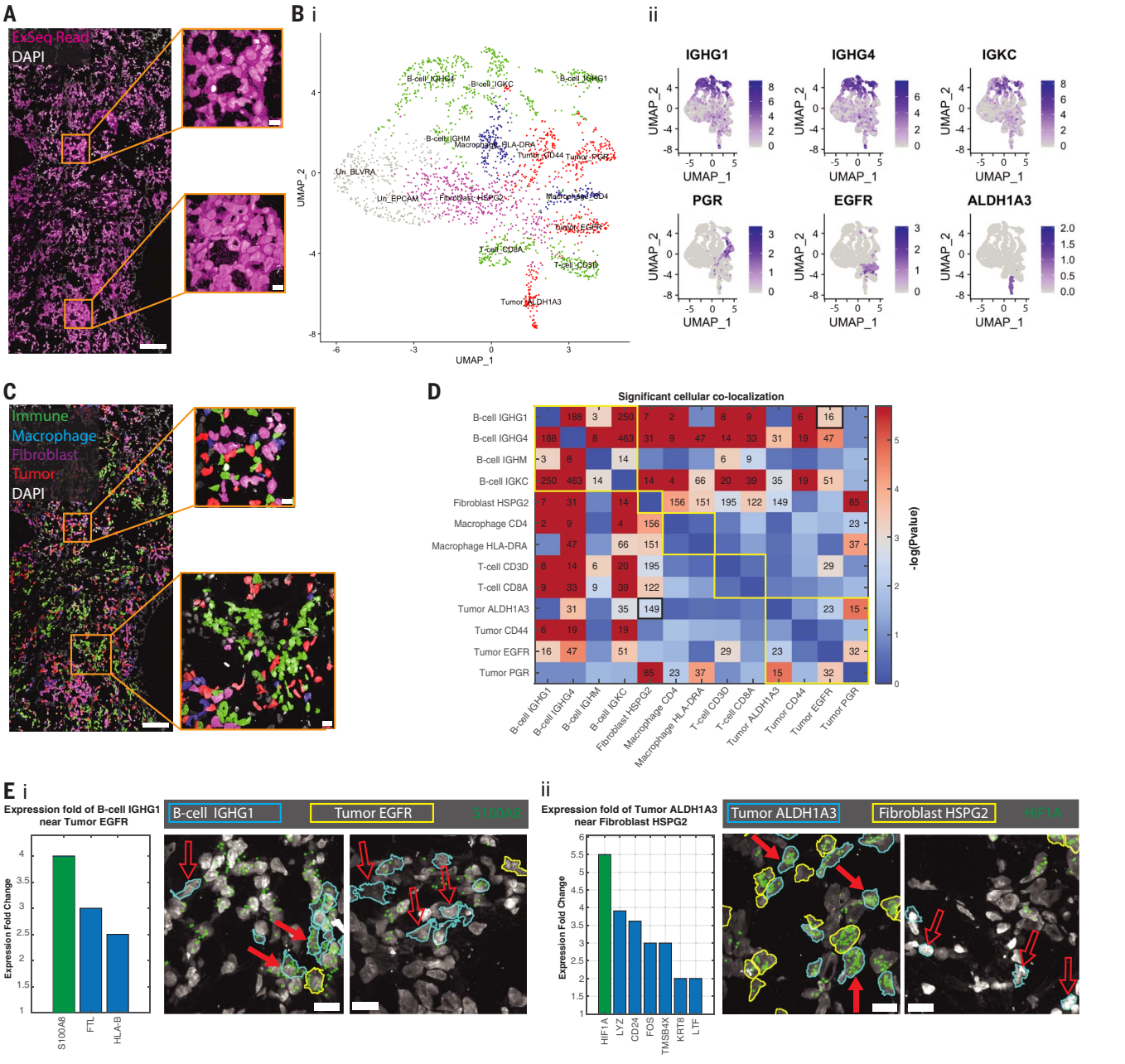

Fig. 6. Targeted ExSeq resolves maps of cell types and states in cancer. (**A**) ExSeq resolves 771,904 reads in 2395 cells (with >100 reads per cell) of 297 genes in a metastatic breast cancer biopsy. (**B**) Uniform manifold approximation and projection (UMAP) representation of principal components analysis (PCA)–based expression clustering reveals immune and tumor cell clusters, indicated by different colors: green (T cells and B cells), red (tumor cells), blue (macrophages), magenta (fibroblasts), and gray [unannotated clusters (*28*)] (i), which express known cell markers for immune cells (ii, top row) and tumor cells (ii, bottom row); expression projected onto UMAP as $\log_2(1 + \text{counts})$. (**C**) Transcriptionally defined cell clusters mapped onto tissue context [colors as in (B)(i)]. (**D**) Spatial colocalization analysis of cell clusters. Adjacency matrix text values, number of cell pairs of indicated type that are in close proximity (nucleus centroid distance of <20 μm; robustness analysis in fig. S26). Adjacency matrix heatmap, *P* value (500,000 bootstrapping iterations), relative to obtaining the same or higher number of cells in close proximity by chance. Adjacency matrix entries with text values are statistically significant (Benjamini Hochberg false-discovery rate of 1.5%). Yellow borders along the diagonal illustrate major cell type categories (B cell, fibroblast, macrophage, T cell, and tumor); the two black-bordered entries correspond to pairs shown in (E). (**E**) ExSeq analysis of cell state as a function of physical proximity, measured by calculating differential expression when cells of different kinds are spatially adjacent (<20 μm) versus far apart. The gene with the largest fold change in a specific cell type when adjacent versus nonadjacent to another specific cell type is shown in green in the histogram ($P = 0.0001$ using 100,000 bootstrapping iterations; all other genes shown in the histogram have $P < 0.05$) as well as in the image showing the gene's read locations in the original sample. (i) Fold change of gene expression in IGHG1-positive B cells when in proximity to EGFR-positive tumor cells (B cells and tumor cells shown with blue and yellow boundaries, respectively). Solid arrows indicate cells in close proximity, and hollow arrows indicate cells not in close proximity. (ii) Fold change of gene expression in ALDH1A3-positive tumor cells when in proximity to HSPG2-positive fibroblasts (tumor and fibroblast cells shown with blue and yellow boundaries, respectively). Scale bars in (A) and (C) are 100 μm, in the insets of (A) and (C) are 10 μm, and in (E) are 10 μm (pre-expansion).

level of *HIF1A* may also indicate tumor radiotherapy resistance (*86*). As a second example, the gene *S100A8*, a regulator of inflammatory processes and immune responses that may be a biomarker for relapse or progression in breast cancer patients (*87*–*89*), was overexpressed fourfold in IGHG1-positive B cells when they were close to EGFR-positive tumor cells (Fig. 6E, i).

Discussion

ExSeq adapts two techniques—ExM and in situ sequencing—to enable spatially precise, highly multiplexed imaging of RNAs in cells and tissues. ExSeq, in both untargeted and targeted forms, facilitates the investigation of scientific questions involving subcellular and even nanoscale RNA localization in intact cellular and tissue contexts (e.g., as indicated by antibody staining of proteins or DAPI staining of nuclei). It can be applied to specimens of multiple-organ systems and species, ranging from the mouse brain to human cancer biopsies, to reveal spatial relationships within and between cells. Such data may reveal principles of cellular organization and function and provide insights into potential mechanisms of how cells interact or are coordinated in complex tissues and multicellular systems. We anticipate that beyond neuroscience and cancer biology, ExSeq will find uses in other fields where many cell types are operating within a complex tissue context—ranging from developmental biology, to immunology, to aging.

Beyond spatial genomics, we expect ExSeq to be useful for in situ sequencing of lineage (*90*) and/or connectome (*91*–*93*) indexing RNA barcodes, which incorporate designed or randomized base-level variation that is not naturally addressed by a FISH approach with a fixed set of tags and targets. More generally, the approaches for re-embedding, passivation, many-round sequential probing, image analysis, and ex situ sequence matching in expanded samples that we have developed for ExSeq should be broadly applicable to other kinds of in situ enzymatic readouts—such as for the multiplexed readout of endogenous DNA or of antibody-attached tags—which may benefit from nanoscale spatial resolution in intact tissues.

Materials and methods summary

All tissues were fixed, optionally immunostained, and treated with the RNA anchoring reagent LabelX. The tissues were then gelled, digested, and expanded (*23*, *26*). Next, the tissues were re-embedded and passivated, which enabled enzymatic reactions to be performed in situ. For untargeted ExSeq, the in situ sequencing library was generated by performing reverse transcription with random primers, circularization of cDNA, and rolling circle amplification (RCA). For targeted ExSeq, padlock probes bearing barcodes were hybridized to transcripts of interest, circularized, and RCA-amplified. In situ sequencing of the cDNA amplicons was then performed through iterative rounds of sequencing chemistry and imaging. The imaging data were converted to nucleotide reads localized in 3D space by a custom image processing pipeline. Reads were ascribed to cells by using immunostaining or other morphological markers. For untargeted ExSeq, the reference for alignment of in situ reads was generated by extracting and sequencing the cDNA amplicons from the sample, which enabled augmentation of the in situ read length. Full materials and methods are available in (*28*).

REFERENCES AND NOTES

1. N. Crosetto, M. Bienko, A. van Oudenaarden, Spatially resolved transcriptomics and beyond. *Nat. Rev. Genet.* **16**, 57–66 (2015). doi: 10.1038/nrg3832; pmid: 25446315
2. T. Gregor, H. G. Garcia, S. C. Little, The embryo as a laboratory: Quantifying transcription in *Drosophila*. *Trends Genet.* **30**, 364–375 (2014). doi: 10.1016/j.tig.2014.06.002; pmid: 25005921
3. S. Alon, G. H. Huynh, E. S. Boyden, Expansion microscopy: Enabling single cell analysis in intact biological systems. *FEBS J.* **286**, 1482–1494 (2019). doi: 10.1111/febs.14597; pmid: 29938896
4. A. E. Moor *et al*., Global mRNA polarization regulates translation efficiency in the intestinal epithelium. *Science* **357**, 1299–1303 (2017). doi: 10.1126/science.aan2399; pmid: 28798045
5. K. B. Halpern *et al*., Single-cell spatial reconstruction reveals global division of labour in the mammalian liver. *Nature* **542**, 352–356 (2017). doi: 10.1038/nature21065; pmid: 28166538
6. E. Lein, L. E. Borm, S. Linnarsson, The promise of spatial transcriptomics for neuroscience in the era of molecular cell typing. *Science* **358**, 64–69 (2017). doi: 10.1126/science.aan6827; pmid: 28983044
7. A. Regev *et al*., The Human Cell Atlas. *eLife* **6**, e27041 (2017). doi: 10.7554/eLife.27041; pmid: 29206104
8. J. R. Moffitt *et al*., Molecular, spatial, and functional single-cell profiling of the hypothalamic preoptic region. *Science* **362**, eaau5324 (2018). doi: 10.1126/science.aau5324; pmid: 30385464
9. S. Shah, E. Lubeck, W. Zhou, L. Cai, In Situ Transcription Profiling of Single Cells Reveals Spatial Organization of Cells in the Mouse Hippocampus. *Neuron* **92**, 342–357 (2016). doi: 10.1016/j.neuron.2016.10.001; pmid: 27764670
10. X. Wang *et al*., Three-dimensional intact-tissue sequencing of single-cell transcriptional states. *Science* **361**, eaat5691 (2018). doi: 10.1126/science.aat5691; pmid: 29930089
11. R. Ke *et al*., In situ sequencing for RNA analysis in preserved tissue and cells. *Nat. Methods* **10**, 857–860 (2013). doi: 10.1038/nmeth.2563; pmid: 23852452
12. A. M. Femino, F. S. Fay, K. Fogarty, R. H. Singer, Visualization of single RNA transcripts in situ. *Science* **280**, 585–590 (1998). doi: 10.1126/science.280.5363.585; pmid: 9554849
13. J. M. Levsky, S. M. Shenoy, R. C. Pezo, R. H. Singer, Single-cell gene expression profiling. *Science* **297**, 836–840 (2002). doi: 10.1126/science.1072241; pmid: 12161654
14. D.-M. Franchini *et al*., Microtubule-Driven Stress Granule Dynamics Regulate Inhibitory Immune Checkpoint Expression in T Cells. *Cell Rep.* **26**, 94–107.e7 (2019). doi: 10.1016/j.celrep.2018.12.014; pmid: 30605689
15. V. Balagopal, R. Parker, Polysomes, P bodies and stress granules: States and fates of eukaryotic mRNAs. *Curr. Opin. Cell Biol.* **21**, 403–408 (2009). doi: 10.1016/j.ceb.2009.03.005; pmid: 19394210
16. C. E. Holt, K. C. Martin, E. M. Schuman, Local translation in neurons: Visualization and function. *Nat. Struct. Mol. Biol.* **26**, 557–566 (2019). doi: 10.1038/s41594-019-0263-5; pmid: 31270476
17. E. M. Schuman, mRNA trafficking and local protein synthesis at the synapse. *Neuron* **23**, 645–648 (1999). doi: 10.1016/S0896-6273(01)80023-4; pmid: 10482231
18. A. J. Rodriguez, K. Czaplinski, J. S. Condeelis, R. H. Singer, Mechanisms and cellular roles of local protein synthesis in mammalian cells. *Curr. Opin. Cell Biol.* **20**, 144–149 (2008). doi: 10.1016/j.ceb.2008.02.004; pmid: 18378131
19. A.-S. Hafner, P. G. Donlin-Asp, B. Leitch, E. Herzog, E. M. Schuman, Local protein synthesis is a ubiquitous feature of neuronal pre- and postsynaptic compartments. *Science* **364**, eaau3644 (2019). doi: 10.1126/science.aau3644; pmid: 31097639
20. C. L. Eng *et al*., Transcriptome-scale super-resolved imaging in tissues by RNA seqFISH. *Nature* **568**, 235–239 (2019). doi: 10.1038/s41586-019-1049-y; pmid: 30911168
21. J. T. Morgan, G. R. Fink, D. P. Bartel, Excised linear introns regulate growth in yeast. *Nature* **565**, 606–611 (2019). doi: 10.1038/s41586-018-0828-1; pmid: 30651636
22. J. H. Lee *et al*., Highly multiplexed subcellular RNA sequencing in situ. *Science* **343**, 1360–1363 (2014). doi: 10.1126/science.1250212; pmid: 24578530
23. F. Chen, P. W. Tillberg, E. S. Boyden, Expansion microscopy. *Science* **347**, 543–548 (2015). doi: 10.1126/science.1260088; pmid: 25592419
24. A. T. Wassie, Y. Zhao, E. S. Boyden, Expansion microscopy: Principles and uses in biological research. *Nat. Methods* **16**, 33–41 (2019). doi: 10.1038/s41592-018-0219-4; pmid: 30573813
25. J. H. Lee *et al*., Fluorescent in situ sequencing (FISSEQ) of RNA for gene expression profiling in intact cells and tissues. *Nat. Protoc.* **10**, 442–458 (2015). doi: 10.1038/nprot.2014.191; pmid: 25675209
26. F. Chen *et al*., Nanoscale imaging of RNA with expansion microscopy. *Nat. Methods* **13**, 679–684 (2016). doi: 10.1038/nmeth.3899; pmid: 27376770
27. G. Wang, J. R. Moffitt, X. Zhuang, Multiplexed imaging of high-density libraries of RNAs with MERFISH and expansion microscopy. *Sci. Rep.* **8**, 4847 (2018). doi: 10.1038/s41598-018-22297-7; pmid: 29555914
28. Detailed materials and methods are available as supplementary materials.
29. A. Kajita, D. Goodwin, R. Prior, dgoodwin208/ExSeqProcessing: First release of the processing software for Expansion Sequencing, version v1.0.0, Zenodo (2020); .doi: 10.5281/zenodo.4075515
30. M. Kircher, P. Heyn, J. Kelso, Addressing challenges in the production and analysis of illumina sequencing data. *BMC Genomics* **12**, 382 (2011). doi: 10.1186/1471-2164-12-382; pmid: 21801405
31. W. Li, J. Freudenberg, P. Miramontes, Diminishing return for increased Mappability with longer sequencing reads: Implications of the k-mer distributions in the human genome. *BMC Bioinformatics* **15**, 2 (2014). doi: 10.1186/1471-2105-15-2; pmid: 24386976
32. P. W. Tillberg *et al*., Protein-retention expansion microscopy of cells and tissues labeled using standard fluorescent proteins and antibodies. *Nat. Biotechnol.* **34**, 987–992 (2016). doi: 10.1038/nbt.3625; pmid: 27376584
33. G. Feng *et al*., Imaging neuronal subsets in transgenic mice expressing multiple spectral variants of GFP. *Neuron* **28**, 41–51 (2000). doi: 10.1016/S0896-6273(00)00084-2; pmid: 11086982
34. J. Svedlund *et al*., Generation of in situ sequencing based OncoMaps to spatially resolve gene expression profiles of diagnostic and prognostic markers in breast cancer. *EBioMedicine* **48**, 212–223 (2019). doi: 10.1016/j.ebiom.2019.09.009; pmid: 31526717
35. K. S. Kosik, Life at Low Copy Number: How Dendrites Manage with So Few mRNAs. *Neuron* **92**, 1168–1180 (2016). doi: 10.1016/j.neuron.2016.11.002; pmid: 28009273
36. M. Khaladkar *et al*., Subcellular RNA sequencing reveals broad presence of cytoplasmic intron-sequence retaining transcripts in mouse and rat neurons. *PLOS ONE* **8**, e76194 (2013). doi: 10.1371/journal.pone.0076194; pmid: 24098440
37. H. Saini, A. A. Bicknell, S. R. Eddy, M. J. Moore, Free circular introns with an unusual branchpoint in neuronal projections. *eLife* **8**, e47809 (2019). doi: 10.7554/eLife.47809; pmid: 31697236
38. P. T. Buckley *et al*., Cytoplasmic intron sequence-retaining transcripts can be dendritically targeted via ID element retrotransposons. *Neuron* **69**, 877–884 (2011). doi: 10.1016/j.neuron.2011.02.028; pmid: 21382548
39. J. Glanzer *et al*., RNA splicing capability of live neuronal dendrites. *Proc. Natl. Acad. Sci. U.S.A.* **102**, 16859–16864 (2005). doi: 10.1073/pnas.0503783102; pmid: 16275927
40. A. Harada, J. Teng, Y. Takei, K. Oguchi, N. Hirokawa, MAP2 is required for dendrite elongation, PKA anchoring in dendrites, and proper PKA signal transduction. *J. Cell Biol.* **158**, 541–549 (2002). doi: 10.1083/jcb.200110134; pmid: 12163474

41. B. Cubelos *et al*., Cux1 and Cux2 regulate dendritic branching, spine morphology, and synapses of the upper layer neurons of the cortex. *Neuron* **66**, 523–535 (2010). doi: 10.1016/j.neuron.2010.04.038; pmid: 20510857
42. P. Crino *et al*., Presence and phosphorylation of transcription factors in developing dendrites. *Proc. Natl. Acad. Sci. U.S.A.* **95**, 2313–2318 (1998). doi: 10.1073/pnas.95.5.2313; pmid: 9482882
43. S. A. Middleton, J. Eberwine, J. Kim, Comprehensive catalog of dendritically localized mRNA isoforms from sub-cellular sequencing of single mouse neurons. *BMC Biol.* **17**, 5 (2019). doi: 10.1186/s12915-019-0630-z; pmid: 30678683
44. L. Pancrazi *et al*., Foxg1 localizes to mitochondria and coordinates cell differentiation and bioenergetics. *Proc. Natl. Acad. Sci. U.S.A.* **112**, 13910–13915 (2015). doi: 10.1073/pnas.1515190112; pmid: 26508630
45. H. Ueda *et al*., Prothymosin alpha-deficiency enhances anxiety-like behaviors and impairs learning/memory functions and neurogenesis. *J. Neurochem.* **141**, 124–136 (2017). doi: 10.1111/jnc.13963; pmid: 28122138
46. H. Tiedge, R. T. Fremeau Jr.., P. H. Weinstock, O. Arancio, J. Brosius, Dendritic location of neural BC1 RNA. *Proc. Natl. Acad. Sci. U.S.A.* **88**, 2093–2097 (1991). doi: 10.1073/pnas.88.6.2093; pmid: 1706516
47. I. A. Muslimov, G. Banker, J. Brosius, H. Tiedge, Activity-dependent regulation of dendritic BC1 RNA in hippocampal neurons in culture. *J. Cell Biol.* **141**, 1601–1611 (1998). doi: 10.1083/jcb.141.7.1601; pmid: 9647652
48. X. Zhang, M. H. Hamblin, K.-J. Yin, The long noncoding RNA Malat1: Its physiological and pathophysiological functions. *RNA Biol.* **14**, 1705–1714 (2017). doi: 10.1080/15476286.2017.1358347; pmid: 28837398
49. J. A. Briggs, E. J. Wolvetang, J. S. Mattick, J. L. Rinn, G. Barry, Mechanisms of Long Non-coding RNAs in Mammalian Nervous System Development, Plasticity, Disease, and Evolution. *Neuron* **88**, 861–877 (2015). doi: 10.1016/j.neuron.2015.09.045; pmid: 26637795
50. H. Hörtnagl *et al*., Patterns of mRNA and protein expression for 12 GABAA receptor subunits in the mouse brain. *Neuroscience* **236**, 345–372 (2013). doi: 10.1016/j.neuroscience.2013.01.008; pmid: 23337532
51. Y. Han *et al*., Up-regulation of Nob1 in the rat auditory system with noise-induced hearing loss. *Neurosci. Lett.* **491**, 79–82 (2011). doi: 10.1016/j.neulet.2011.01.010; pmid: 21219967
52. N. Schneider, M. Meier, Efficient in situ detection of mRNAs using the Chlorella virus DNA ligase for padlock probe ligation. *RNA* **23**, 250–256 (2017). doi: 10.1261/rna.057836.116vpmid: 27879431
53. D. Fürth, V. Hatini, J. H. Lee, In Situ Transcriptome Accessibility Sequencing (INSTA-seq). bioRxiv 722819 [Preprint]. 6 August 2019. .doi: 10.1101/722819
54. A. E. Cartier *et al*., Regulation of synaptic structure by ubiquitin C-terminal hydrolase L1. *J. Neurosci.* **29**, 7857–7868 (2009). doi: 10.1523/JNEUROSCI.1817-09.2009; pmid: 19535597
55. G. J. S. Lohman, Y. Zhang, A. M. Zhelkovsky, E. J. Cantor, T. C. Evans Jr.., Efficient DNA ligation in DNA-RNA hybrid helices by Chlorella virus DNA ligase. *Nucleic Acids Res.* **42**, 1831–1844 (2014). doi: 10.1093/nar/gkt1032; pmid: 24203707
56. R. Deng, K. Zhang, Y. Sun, X. Ren, J. Li, Highly specific imaging of mRNA in single cells by target RNA-initiated rolling circle amplification. *Chem. Sci.* **8**, 3668–3675 (2017). doi: 10.1039/C7SC00292K; pmid: 28580104
57. E. P. R. Iyer *et al*., Barcoded oligonucleotides ligated on RNA amplified for multiplex and parallel in-situ analyses. bioRxiv 281121 [Preprint]. 20 March 2018. .doi: 10.1101/281121
58. H. M. T. Choi *et al*., Third-generation *in situ* hybridization chain reaction: Multiplexed, quantitative, sensitive, versatile, robust. *Development* **145**, dev165753 (2018). doi: 10.1242/dev.165753; pmid: 29945988
59. G. K. Marinov *et al*., From single-cell to cell-pool transcriptomes: Stochasticity in gene expression and RNA splicing. *Genome Res.* **24**, 496–510 (2014). doi: 10.1101/gr.161034.113; pmid: 24299736
60. E. Torre *et al*., Rare Cell Detection by Single-Cell RNA Sequencing as Guided by Single-Molecule RNA FISH. *Cell Syst.* **6**, 171–179.e5 (2018). doi: 10.1016/j.cels.2018.01.014; pmid: 29454938
61. B. Tasic *et al*., Adult mouse cortical cell taxonomy revealed by single cell transcriptomics. *Nat. Neurosci.* **19**, 335–346 (2016). doi: 10.1038/nn.4216; pmid: 26727548
62. L. van der Maaten, G. Hinton, Visualizing Data using t-SNE. *J. Mach. Learn. Res.* **9**, 2579–2605 (2008); http://jmlr.org/papers/v9/vandermaaten08a.html.
63. E. S. Lein *et al*., Genome-wide atlas of gene expression in the adult mouse brain. *Nature* **445**, 168–176 (2007). doi: 10.1038/nature05453; pmid: 17151600
64. L. E. Ostroff, J. C. Fiala, B. Allwardt, K. M. Harris, Polyribosomes redistribute from dendritic shafts into spines with enlarged synapses during LTP in developing rat hippocampal slices. *Neuron* **35**, 535–545 (2002). doi: 10.1016/S0896-6273(02)00785-7; pmid: 12165474
65. O. Steward, P. Worley, Local synthesis of proteins at synaptic sites on dendrites: Role in synaptic plasticity and memory consolidation? *Neurobiol. Learn. Mem.* **78**, 508–527 (2002). doi: 10.1006/nlme.2002.4102; pmid: 12559831
66. Y. J. Yoon *et al*., Glutamate-induced RNA localization and translation in neurons. *Proc. Natl. Acad. Sci. U.S.A.* **113**, E6877–E6886 (2016). doi: 10.1073/pnas.1614267113; pmid: 27791158
67. I. J. Cajigas *et al*., The local transcriptome in the synaptic neuropil revealed by deep sequencing and high-resolution imaging. *Neuron* **74**, 453–466 (2012). doi: 10.1016/j.neuron.2012.02.036; pmid: 22578497
68. A. Y. Hung *et al*., Smaller dendritic spines, weaker synaptic transmission, but enhanced spatial learning in mice lacking Shank1. *J. Neurosci.* **28**, 1697–1708 (2008). doi: 10.1523/JNEUROSCI.3032-07.2008; pmid: 18272690
69. N. Hirokawa, S. Niwa, Y. Tanaka, Molecular motors in neurons: Transport mechanisms and roles in brain function, development, and disease. *Neuron* **68**, 610–638 (2010). doi: 10.1016/j.neuron.2010.09.039; pmid: 21092854
70. A. J. Koleske, Molecular mechanisms of dendrite stability. *Nat. Rev. Neurosci.* **14**, 536–550 (2013). doi: 10.1038/nrn3486; pmid: 23839597
71. O. Steward, C. S. Wallace, G. L. Lyford, P. F. Worley, Synaptic activation causes the mRNA for the IEG Arc to localize selectively near activated postsynaptic sites on dendrites. *Neuron* **21**, 741–751 (1998). doi: 10.1016/S0896-6273(00)80591-7; pmid: 9808461
72. O. Steward, P. F. Worley, Selective targeting of newly synthesized Arc mRNA to active synapses requires NMDA receptor activation. *Neuron* **30**, 227–240 (2001). doi: 10.1016/S0896-6273(01)00275-6; pmid: 11343657
73. D. S. Chen, I. Mellman, Elements of cancer immunity and the cancer-immune set point. *Nature* **541**, 321–330 (2017). doi: 10.1038/nature21349; pmid: 28102259
74. P. L. Ståhl *et al*., Visualization and analysis of gene expression in tissue sections by spatial transcriptomics. *Science* **353**, 78–82 (2016). doi: 10.1126/science.aaf2403; pmid: 27365449
75. S. G. Rodriques *et al*., Slide-seq: A scalable technology for measuring genome-wide expression at high spatial resolution. *Science* **363**, 1463–1467 (2019). doi: 10.1126/science.aaw1219; pmid: 30923225
76. M. Fenech *et al*., Molecular mechanisms of micronucleus, nucleoplasmic bridge and nuclear bud formation in mammalian and human cells. *Mutagenesis* **26**, 125–132 (2011). doi: 10.1093/mutage/geq052; pmid: 21164193
77. T. Stuart *et al*., Comprehensive Integration of Single-Cell Data. *Cell* **177**, 1888–1902.e21 (2019). doi: 10.1016/j.cell.2019.05.031; pmid: 31178118
78. M. Kitahara *et al*., HER2-Positive Conversion in a Metastatic Liver Focus in Late Recurrent Breast Cancer. *Case Rep. Oncol.* **12**, 473–479 (2019). doi: 10.1159/000501306; pmid: 31320870
79. H. Masuda *et al*., Role of epidermal growth factor receptor in breast cancer. *Breast Cancer Res. Treat.* **136**, 331–345 (2012). doi: 10.1007/s10549-012-2289-9; pmid: 23073759
80. P. Marcato *et al*., Aldehyde dehydrogenase activity of breast cancer stem cells is primarily due to isoform ALDH1A3 and its expression is predictive of metastasis. *Stem Cells* **29**, 32–45 (2011). doi: 10.1002/stem.563; pmid: 21280157
81. S. Garaud *et al*., Tumor-infiltrating B cells signal functional humoral immune responses in breast cancer. *JCI Insight* **4**, e129641 (2019). doi: 10.1172/jci.insight.129641; pmid: 31408436
82. E. Pipi *et al*., Tertiary Lymphoid Structures: Autoimmunity Goes Local. *Front. Immunol.* **9**, 1952 (2018). doi: 10.3389/fimmu.2018.01952; pmid: 30258435
83. S. Nayar *et al*., Immunofibroblasts are pivotal drivers of tertiary lymphoid structure formation and local pathology. *Proc. Natl. Acad. Sci. U.S.A.* **116**, 13490–13497 (2019). doi: 10.1073/pnas.1905301116; pmid: 31213547
84. M. Bartoschek *et al*., Spatially and functionally distinct subclasses of breast cancer-associated fibroblasts revealed by single cell RNA sequencing. *Nat. Commun.* **9**, 5150 (2018). doi: 10.1038/s41467-018-07582-3; pmid: 30514914
85. N. Colwell *et al*., Hypoxia in the glioblastoma microenvironment: Shaping the phenotype of cancer stem-like cells. *Neuro-Oncol.* **19**, 887–896 (2017). doi: 10.1093/neuonc/now258; pmid: 28339582
86. F. Cimmino *et al*., HIF-1 transcription activity: HIF1A driven response in normoxia and in hypoxia. *BMC Med. Genet.* **20**, 37 (2019). doi: 10.1186/s12881-019-0767-1; pmid: 30808328
87. C. Gebhardt, J. Németh, P. Angel, J. Hess, S100A8 and S100A9 in inflammation and cancer. *Biochem. Pharmacol.* **72**, 1622–1631 (2006). doi: 10.1016/j.bcp.2006.05.017; pmid: 16846592
88. J.-M. Zhong *et al*., Protein S100-A8: A potential metastasis-associated protein for breast cancer determined via iTRAQ quantitative proteomic and clinicopathological analysis. *Oncol. Lett.* **15**, 5285–5293 (2018). doi: 10.3892/ol.2018.7958; pmid: 29552168
89. D. Wang *et al*., Clinical Significance of Elevated S100A8 Expression in Breast Cancer Patients. *Front. Oncol.* **8**, 496 (2018). doi: 10.3389/fonc.2018.00496; pmid: 30456203
90. R. Kalhor *et al*., Developmental barcoding of whole mouse via homing CRISPR. *Science* **361**, eaat9804 (2018). doi: 10.1126/science.aat9804; pmid: 30093604
91. X. Chen, Y.-C. Sun, G. M. Church, J. H. Lee, A. M. Zador, Efficient in situ barcode sequencing using padlock probe-based BaristaSeq. *Nucleic Acids Res.* **46**, e22 (2018). doi: 10.1093/nar/gkx1206; pmid: 29190363
92. I. D. Peikon *et al*., Using high-throughput barcode sequencing to efficiently map connectomes. *Nucleic Acids Res.* **45**, e115 (2017). doi: 10.1093/nar/gkx292; pmid: 28449067
93. A. M. Zador *et al*., Sequencing the connectome. *PLOS Biol.* **10**, e1001411 (2012). doi: 10.1371/journal.pbio.1001411; pmid: 23109909
94. D. Goodwin, dgoodwin208/ExSeqOF3DVisualizer: First release of 3D visualization software for Expansion Sequencing, version v1.0.0, Zenodo (2020); .doi: 10.5281/zenodo.4075649

ACKNOWLEDGMENTS

We acknowledge A. Lin for the help with Illumina sequencing, D. Park for providing cultured neurons, E. Murray for providing cultured HeLa cells, K. Piatkevich for performing transcardial perfusions, R. Kalhor for helpful discussions, and E. A. Pnevmatikakis for helpful discussions on image processing. We also acknowledge the SpaceTx analysis working group for help in clustering (T. Bakken, Z. Yao, and P. Kharchenko) and for help in gene selection (E. D. Vaishnav, B. Aevermann, R. Scheuermann, and K. Harris). **Funding:** R.E.K. and A.H.M. acknowledge IARPA MICrONS (D16PC0008); E.R.D. acknowledges government support under HG005550 and HG008525 awarded by the National Institutes of Health and under DGE1144152 awarded by the National Science Foundation; S.A. was supported by the Howard Hughes Medical Institute (HHMI) fellowship of the LSRF; D.R.G. is an NSF GRFP fellow; F.C. is supported by the Schmidt Fellows Program at the Broad Institute; A.T.W. was supported by the Hertz Foundation Fellowship and the Siebel Scholarship; A.S. was supported by the NIH Neuroimaging Training Program T32 grant 5T32EB001680; and J.A.M. and E.S.L. thank the Chan Zuckerberg Initiative, an advised fund of Silicon Valley Community Foundation, for their support (award no. 2017-0525). E.S.B. was supported by L. Yang, J. Doerr, the Open Philanthropy Project, Cancer Research UK Grand Challenge grant C31893/A25050, U.S. Army Research Laboratory and the U.S. Army Research Office under contract no. W911NF1510548, NSF grant 1734870, NIH UF1NS107697, NIH IDIQ17X149, NIH 1RM1HG008525, NIH 1R01MH103910, NIH 1R01MH114031, NIH 1R01MH110932, NIH 1R01EB024261, NIH 1R01DA045549, IARPA D16PC00008, NIH 1U19MH114821, NIH 1R01NS102727, the Chan Zuckerberg Initiative Human Cell Atlas pilot program, the Ludwig Foundation, the HHMI-Simons Faculty Scholars Program, and the HHMI investigator program. This project has been funded in part with federal funds from the National Cancer Institute, National Institutes of Health, task order no. HHSN261100039 under contract no. HHSN261201500003I. J.K. was supported by an HFSP long-term fellowship (LT000452/2019-L). **Author contributions:** S.A., D.R.G., A.S., A.T.W., F.C., E.R.D., G.M.C., A.H.M., and E.S.B. contributed key ideas and designed experiments; S.A., A.T.W., A.S., and F.C. performed experiments; S.A., D.R.G., A.T.W., A.S., F.C., A.H.M., and E.S.B. analyzed data and wrote the paper; D.R.G., F.C., Y.B., A.K., and A.G.X. conceived and implemented the image analysis pipeline with assistance from S.A. and initial discussions with E.R.D; D.R.G., Y.B., A.K., A.G.X., K.M., and R.P. analyzed the imaging data; A.T.W., A.S., F.C., and A.H.M. conceived and implemented targeted ExSeq;

D.R.G. designed and implemented the 3D visualization tool; D.R.G. analyzed cDNA movement experiments; S.A. and D.R.G. performed 3D tracing; Y.C., A.C.P., C.-C.Ya., P.T., P.R., and R.E.K. contributed to protocol optimization; S.A., F.C., H.-J.S., and R.W. automated the in situ sequencing; F.C., E.R.D., and A.H.M. conceived passivation; S.A. and F.C. implemented passivation; S.A. and F.C. conceived and implemented ex situ sequencing with initial discussions with E.R.D and A.C.P.; S.A. and F.C. implemented ex situ and in situ sequencing matching with assistance from D.R.G.; S.A., A.T.W., A.S., and F.C. conceived and implemented antibody staining; E.R.D. conceived and implemented cDNA fragmentation protocol and performed experiments on earlier preliminary protocols; S.A., F.C., and E.R.D. optimized FISSEQ enzymatics for the expanded gel; S.A. and F.C. conceived and implemented cDNA anchoring with initial discussions with E.R.D.; C.-C.Yu performed *C. elegans* fixation, cuticle reduction, and permeabilization; N.P. carried out mouse surgeries; J.A.M. and E.S.L. designed the gene list for the visual cortex experiment; A.L., N.C., S.R., K.H., D.L.A., N.W., B.E.J., J.K., M.S., J.W., J.J.-V., O.R.-R., and A.R. designed the gene list and provided the human sample for the cancer experiment; S.L., S.P., and E.P.R.I. contributed to targeted ExSeq; A.H.M., E.S.B., and G.M.C. initiated the project; and E.S.B. supervised the project. **Competing interests:** E.S.B. is a cofounder of Expansion Technologies, which has commercial interests in the space of ExM. F.C. is a paid consultant of Celsius Therapeutics and is a member of Celsius Thinklab. E.R.D. is a cofounder of ReadCoor, part of 10x Genomics, which has commercial interests in the space of ExM and FISSEQ. From October 2019, A.L. is an employee of Bristol Myers Squibb. From June 2018, E.P.R.I. is an employee of 10x Genomics. N.W. is a stockholder of Relay Therapeutics, is in the scientific advisory board of Relay Therapeutics, is a consultant to Eli Lilly, and received a grant from Puma Biotechnologies. A.R. is a founder and equity holder of Celsius Therapeutics; an equity holder in Immunitas Therapeutics; and, until 31 August 2020, was an SAB member of Syros Pharmaceuticals, Neogene Therapeutics, Asimov, and ThermoFisher Scientific. From 1 August 2020, A.R. is an employee of Genentech, a member of the Roche Group. G.M.C. is a cofounder and SAB member of ReadCoor and is an adviser to 10x Genomics after their acquisition of ReadCoor. Conflict of interest link for G.M.C.: http://arep.med.harvard.edu/gmc/tech.html. S.A., D.R.G., A.T.W., A.S., F.C., E.R.D., A.C.P., P.T., G.M.C., A.H.M., and E.S.B. are inventors on U.S. patents 10526649, 10364457, and 10059990 and U.S. patent application 15/876,347, submitted by MIT and Harvard, that cover ExSeq. **Data and materials availability:** All of the raw Illumina sequencing data were deposited to the National Center for Biotechnology Information (NCBI) Sequence Read Archive (SRA), BioProject PRJNA663046. The entire MATLAB pipeline to process ExSeq datasets from the microscope to spatial analysis of gene expression is publicly accessible at Zenodo (*29*). From there, a tutorial with step-by-step instructions on how to run the pipeline and a tutorial set of targeted ExSeq data from the mouse visual cortex can be accessed. The 3D visualization tool is hosted at Zenodo (*94*).

SUPPLEMENTARY MATERIALS

science.sciencemag.org/content/371/6528/eaax2656/suppl/DC1
IMAXT Consortium Collaborator List
Materials and Methods
Figs. S1 to S26
Tables S1 to S14
References (*95*–*137*)
MDAR Reproducibility Checklist

View/request a protocol for this paper from *Bio-protocol*.

8 March 2019; resubmitted 13 May 2020
Accepted 20 November 2020
10.1126/science.aax2656

Science

Expansion sequencing: Spatially precise in situ transcriptomics in intact biological systems

Shahar Alon, Daniel R. Goodwin, Anubhav Sinha, Asmamaw T. Wassie, Fei Chen, Evan R. Daugharthy, Yosuke Bando, Atsushi Kajita, Andrew G. Xue, Karl Marrett, Robert Prior, Yi Cui, Andrew C. Payne, Chun-Chen Yao, Ho-Jun Suk, Ru Wang, Chih-Chieh (Jay) Yu, Paul Tillberg, Paul Reginato, Nikita Pak, Songlei Liu, Sukanya Punthambaker, Eswar P. R. Iyer, Richie E. Kohman, Jeremy A. Miller, Ed S. Lein, Ana Lako, Nicole Cullen, Scott Rodig, Karla Helvie, Daniel L. Abravanel, Nikhil Wagle, Bruce E. Johnson, Johanna Klughammer, Michal Slyper, Julia Waldman, Judit Jané-Valbuena, Orit Rozenblatt-Rosen, Aviv Regev, IMAXT Consortium, George M. Church, Adam H. Marblestone and Edward S. Boyden

Science **371** (6528), eaax2656.
DOI: 10.1126/science.aax2656

Identifying transcript location in cells

Identifying where specific RNAs occur within a cell or tissue has been limited by technology and imaging capabilities. Expansion microscopy has allowed for better visualization of small structures by expanding the tissues with a polymer- and hydrogel-based system. Alon *et al.* combined expansion microscopy with long-read in situ RNA sequencing, resulting in a more precise visualization of the location of specific transcripts. This method, termed "ExSeq" for expansion sequencing, was used to detect RNAs, both new transcripts and those previously demonstrated to localize to neuronal dendrites. Unlike other in situ sequencing methods, ExSeq does not target sets of genes. This technology thus unites spatial resolution, multiplexing, and an unbiased approach to reveal insights into RNA localization and its physiological roles in developing and active tissue.

Science, this issue p. eaax2656